nature communications

Article

https://doi.org/10.1038/s41467-025-57632-w

Senescent-like microglia limit remyelination through the senescence associated secretory phenotype

Received: 17 May 2024

Accepted: 24 February 2025

Published online: 07 March 2025

Check for updates

Phillip S. Gross[1,2], Violeta Durán-Laforet[3], Lana T. Ho[4], George S. Melchor[1,2], Sameera Zia[5], Zeeba Manavi[2], William E. Barclay[6], Sung Hyun Lee[2], Nataliia Shults[2], Sean Selva[7], Enrique Alvarez[7], Jason R. Plemel[5], Meng-meng Fu[4,6], Dorothy P. Schafer[3] & Jeffrey K. Huang[1,2]

The capacity to regenerate myelin in the central nervous system diminishes with age. This decline is particularly evident in multiple sclerosis (MS), a chronic demyelinating disease. Whether cellular senescence, a hallmark of aging, contributes to remyelination impairment remains unknown. Here, we show that senescent cells accumulate within demyelinated lesions after injury, and treatments with senolytics enhances remyelination in young and middle-aged mice but not aged mice. In young mice, we observe the upregulation of senescence-associated transcripts, primarily in microglia and macrophages, after demyelination, followed by a reduction during remyelination. However, in aged mice, senescence-associated factors persist within lesions, correlating with inefficient remyelination. Proteomic analysis of the senescence-associated secretory phenotype (SASP) reveals elevated levels of CCL11/Eotaxin-1 in lesions of aged mice, which is found to inhibit oligodendrocyte maturation. These results suggest therapeutic targeting of SASP components, such as CCL11, may improve remyelination in aging and MS.

Multiple Sclerosis (MS) is a chronic, immune-mediated demyelinating disease, in which immune cells infiltrate the central nervous system (CNS) and promote the deterioration of myelin and oligodendrocytes, resulting in denuded axons and progressive neurodegeneration[1]. Early in the disease, oligodendrocyte precursor cells (OPCs) migrate to the site of the demyelinated lesions and differentiate into mature myelinating oligodendrocytes, a regenerative process termed remyelination[2]. However, with age, remyelination becomes inefficient[3,4]. This is mirrored in the clinical disease course, where for reasons that remain poorly understood, patients typically transition from Relapse Remitting MS (RRMS) to Secondary Progressive MS (SPMS), which is characterized by the progressive worsening of symptoms[5–7]. Similarly, patients with Primary Progressive MS (PPMS) are typically initially diagnosed at similar ages as SPMS initiation[8,9], leading to speculation that they may represent the same disease form, collectively referred as Progressive MS (PMS). One potential reason for disease progression is the failure of the remyelination process to keep pace with demyelination, leading to progressive axonal dystrophy and neurodegeneration. Notably, therapeutics for MS predominantly rely on modifying the immune system during RRMS, with a limited focus on improving remyelination. Further, most therapeutics become ineffective once the patient progresses, which usually occurs during middle age regardless of disease duration[8,10,11]. Since PMS onset is associated with increasing age, we hypothesized that the accumulation

[1]Interdisciplinary Program in Neuroscience, Georgetown University, Washington, DC, USA. [2]Department of Biology, Georgetown University, Washington, DC, USA. [3]Department of Neurobiology, Brudnick Neuropsychiatric Research Institute, University of Massachusetts Chan Medical School, Worcester, MA, USA. [4]Department of Molecular and Cell Biology (MCB), University of California Berkeley, Berkeley, CA, USA. [5]Neuroscience and Mental Health Institute, University of Alberta, Edmonton, Canada. [6]National Institute of Neurological Disorders and Stroke, National Institutes of Health, Bethesda, MD, USA. [7]Department of Neurology, University of Colorado Anschutz Medical Campus, Aurora, CO, USA. e-mail: jh1659@georgetown.edu

of senescent cells (SCs) with age limits remyelination, resulting in increased neurodegeneration and clinical deterioration.

SCs are cells locked in cell cycle arrest that become resistant to apoptosis, and release a heterogenous milieu of inflammatory factors termed the senescence associated secretory phenotype (SASP)[12,13]. Often associated with increasing age, these cells have been implicated in multiple age-related neurodegenerative diseases[14,15]. The selective clearance of SCs in mouse models results in alleviation of disease symptoms and progression[16–18], extension of lifespan[19,20], and improved healthspan[21,22]. Interestingly, MS has been shown to affect chronological aging[23], and recent evidence of SCs in MS lesions has been reported[24–27]. However, the impact of SCs on remyelination efficiency remains unknown.

Here, we show the upregulation of the senescence marker P16^{ink4a} (P16) in microglial and macrophage cells in demyelinated lesions following acute demyelination and its gradual decline during efficient remyelination in mice. We also show P16+ microglia in demyelinated lesions increase and persist in lesions with advancing age. Furthermore, we detect low levels of cellular senescence in oligodendrocyte lineage cells. Using Multiplexed Error-Robust Fluorescence In Situ Hybridization (MERFISH) and protein multiplexing, we find that young and aged mouse lesions display transcripts associated with cellular senescence and neuroinflammation, with higher expression in aged mice. Notably, treatment of SCs using genetic and pharmacological senolytic methods leads to enhanced remyelination in young and middle-aged mice but fails to improve remyelination in aged mice. RNA-sequencing and protein multiplexing analyses revealed treatment with senolytics reduces the levels of SASP proteins within aged lesions. We identified CCL11/Eotaxin-1 as one of the major SASP factors increased in aged lesions and altered by treatment with senolytics. Moreover, we find elevated CCL11 levels correlate with disease severity in MS and inhibit oligodendrocyte maturation in vitro. Furthermore, inhibiting CCL11 in mice partially mimics the beneficial effects of treatment with senolytics on remyelination. Our results suggest SCs limit remyelination through the accumulation of SASP in demyelinated lesions, and that inhibition of SASP, such as CCL11, may increase remyelination efficiency by fostering a more favorable regenerative environment.

Results

Senescent cells are found within demyelinated lesions

Senescent cells (SC) have been observed in the brains of individuals with multiple sclerosis (MS), but their impact on the remyelination process remains unclear. To determine if SCs are detectable in demyelinated lesions in mice, focal demyelination by injection of lysophosphatidylcholine (LPC) was performed on spinal cord white matter of young adult mice (3 months old) (Fig. 1a). This approach induces acute demyelination, with lesions identified by hyper-nucleation, which inversely stains myelinated regions in spinal cord white matter sections (Fig. 1b), and subsequently results in remyelination in a predictable manner with timepoints at 5 days post lesion (dpl) (corresponding with inflammation and OPC recruitment), 10 dpl (corresponding with inflammation resolution and OPC differentiation), 20 dpl (corresponding with completion of remyelination), and 60 dpl (corresponding with extended oligodendrocyte myelination)[28,29] (Fig. 1c). To quantify the level of SCs in lesions during remyelination, we used P16-tdTomato (p16tdt) mice, which express a tdTomato reporter under the endogenous promotor of *P16^{ink4a}*, a key gene in senescence programming[30] (Fig. 1d). We found that compared to naive control white matter, which exhibits very low p16tdt expression (Supplementary Fig. 1a), demyelinated lesions showed a substantial increase in p16tdt expression at 5 dpl followed by a gradual decrease at 10, 20, and 60 dpl (Fig. 1e, f).

To confirm the observed transient timecourse of senescent cell activity, we reanalyzed a recently generated single-nucleus RNA-sequencing data of mouse lesions undergoing remyelination[31] for SenMayo gene expression, a geneset of differentially expressed genes in senescent cells[32]. In agreement with our immunofluorescent data, we found a peak in SenMayo gene expression scores in the lesion at 5 dpl, followed by a return to baseline at 10 and 20 dpl (Fig. 1g). This pattern was further supported by *Cdkn2a (P16)* expression in this snRNA-Seq dataset, which closely mirrored the timecourse of p16-tdt staining and SenMayo gene expression (Fig. 1h). As expected, the observed peak of senescence at 5 dpl followed by reduction at 10 and 20 dpl inversely correlated with gene expression associated with oligodendrocyte maturation and myelination, which is lowest at 5 dpl and peaked at 10 and 20 dpl (Supplementary Fig 1b). Together, these observations suggest that senescent cell activity within lesions is transient under efficient remyelinating conditions.

Since 5 dpl was confirmed to be the peak of senescence during remyelination, we focused our analyses primarily on 5 and 10 dpl. Using IVIS imaging, we observed increased bioluminescence in spinal cord lesions of p16tdt mice compared to LPC-lesioned wildtype or sham lesioned (briefly exposed spinal cord) p16tdt mice (Fig. 1i and Supplementary Fig. 1c, d). Moreover, RT-qPCR analysis of demyelinated lesions at 5 dpl revealed upregulation of *P16/Cdkn2a* and *Rb1*, genes associated with cellular senescence, downregulation of *Tert*, associated with a youthful cell state, and upregulation of *Apoe* and *Trem2*, associated with disease-associated microglia (DAM) compared to naive control (Supplementary Fig. 1e). Additionally, there was a slight, but significant downregulation of *P21/Cdkn1a* and no difference in *Trp53* and *E2f1* (Supplementary Fig. 1e).

To determine which cell population(s) exhibit cellular senescence in demyelinated lesions, we co-stained p16tdt with markers of myeloid cells (CD11b), astrocytes (GFAP), mature oligodendrocytes (CC1) and OPCs (Nkx2.2) (Fig. 1j–m). We found p16tdt predominantly co-localized with CD11b+ cells in lesions (Fig. 1n and Supplementary Fig. 2a, h, i), accounting for 62% of the p16tdt+ cells (Fig. 1o), and 20% of the myeloid cells in the lesion (Fig. 1p). Although Cd11b does not distinguish between peripheral myeloid cells and microglia in lesions, previous lineage tracing experiments indicate that microglia are the predominant immune cells in the lesions by 10 dpl[33,34]. Additionally, co-immunostaining analysis for p16tdt and SALL1, a microglia-associated marker[35], suggests the senescent myeloid cells observed in lesions are likely derived from microglia (Supplementary Fig. 2a–c). Furthermore, we observed low expression of p16tdt in oligodendrocyte progenitors and oligodendrocytes (Fig. 1n and Supplementary Fig. 2a, d–g). Additionally, reanalysis of single-nucleus RNA-sequencing data from mouse lesions during remyelination[31] revealed myeloid cell- specific SenMayo scores and Cdkn2a/P16 and Cdkn1a/P21 gene expression all mirrored the overall lesion senescence expression time course, peaking at 5 days post-lesion (dpl) (Supplementary Fig. 2j–l). Taken together, our findings suggest that cellular senescence increases primarily in microglia and macrophages within demyelinated lesions, which naturally decreases during efficient remyelination in young adult mice.

Chronic active lesions in MS often exhibit increased microglial activation, which is associated with impaired remyelination[25]. Further, it has been shown that P16 could be observed in microglia within the brains of individuals with MS[25] and recently senolytic treatment in a mouse model of MS resulted in reduced microglia and disease severity[27]. To determine if microglial senescence occurs in MS, we re-analyzed microglia in a previously published single nucleus RNA sequencing (snRNA-seq) database of MS lesions[36]. We detected an elevation of *CDKN2A/P16* and senescence scores in microglia in both chronic active and inactive MS lesions compared to control brain tissues (Fig. 1q–s and Supplementary Fig. 3a). Interestingly, *CDKN2A*+ and *CDKN2A*- microglia also expressed varying levels of other senescent genes, indicating a potential transcriptional heterogeneity among senescent microglia (Supplementary Fig. 3b, c). Notably, we observed that microglia with a high senescence score in MS lesions (Fig. 1r)

https://doi.org/10.1038/s41467-025-57632-w

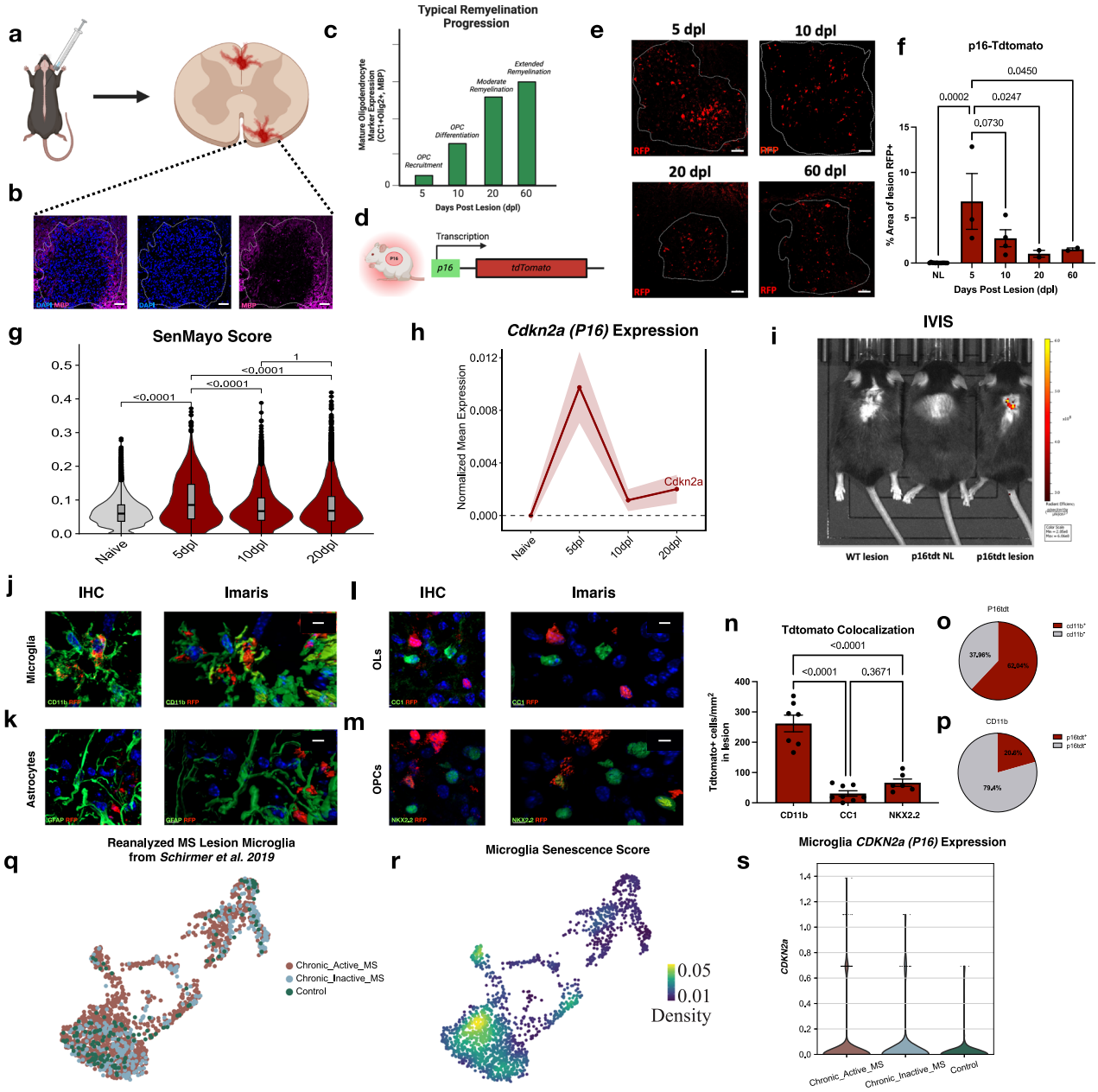

Fig. 1 | Senescent microglia/macrophages following demyelination. a Schematic of lysophosphatidylcholine (LPC) induced demyelination. **b** Lesions identified in all experiments by hyper-nucleated regions of white matter which inversely reflect myelination (MBP). **c** Typical progression of remyelination at specified time points following LPC-induced lesions. **d** Schematic of p16-tdTomato mouse model. **e** Immunofluorescent staining of p16tdt+ cells throughout remyelination in 3 months old mice (dpl: days post lesion). **f** Quantification of (**e**) ($n = 13$ NL, 3 5dpl, 4 10dpl, 2 20dpl, 2 60dpl; each n denotes biologically independent replicate). **g** Violin plots depicting the SenMayo geneset score in the naive mouse spinal cord ($n = 2$) and at 5 ($n = 3$), 10 ($n = 2$), and 20 ($n = 3$) dpl from reanalyzed snRNA-sequencing data (n denotes biologically independent replicate; 7872 nuclei per timepoint). Boxplots show distribution of geneset score at the single nucleus level and statistical information is in source Data file. **h** Line graph indicating the normalized mean expression of *Cdkn2a/P16* across all cells in naïve samples, and at 5, 10, and 20dpl in (**g**). Line graphs are 95% confidence interval. **i** In Vivo Imaging System (IVIS) bioluminescence of controls and p16tdt lesions ($n = 1$ WT, 1 Sham L, 2 p16tdt L). **j**–**m** Immunofluorescent (IHC) staining and Imaris 3D reconstruction of p16tdt and CD11b, GFAP, CC1, and NKX2.2 colocalization. **n** Quantification of (**j**–**m**) ($n = 7$ CD11b, 8 CC1, 6 NKX2.2; each n denotes biologically independent replicate). **o**, **p** Percentages of p16tdt+ cells CD11b+ and CD11b+ cells p16tdt + . **q** Uniform manifold approximation and projection (UMAP) visualization of re-analyzed microglia from snRNA-sequencing of chronic active lesions, inactive lesions, and control samples (1815 total microglia). **r** UMAP showing the weighted gene density estimation of the senescence score, aggregate sum expression of genes found in Supplementary data 1. **s** Violin plots describing expression levels of *P16/Cdkn2a* in microglia in chronic active lesions, inactive lesions, and control samples ($n = 1321$, 349, 145 microglia, respectively). Data are mean ± SEM (**f**, **n**) or median (**g**). Scale bar, 50 μm (**b**, **e**), 5 μm (**k**, **l**) 1 μm (**j**, **m**). *P* values derived from one-way ANOVA with Tukey corrected multiple comparisons (**f**, **n**), or the two-tailed Wilcoxon test followed by Bonferroni correction (**g**). Select figures created in BioRender (2025) (**a**, **d**) https://BioRender.com/r92t091, (**c**) https://BioRender.com/b11w175. Source data are provided as a Source Data file.

expressed elevated levels of *TNFRSF1a, TCTEX1D1, LYZ2*, and *EOGT* (Supplementary Fig. 3d). This microglial subset appears to be present predominantly in chronic active lesions, indicating senescence activity remains elevated under chronic inflammation in MS.

Persistence of senescent cells are associated with inefficient remyelination in aged mice

As remyelination becomes less efficient with age, we next asked if the presence of SCs in demyelinated lesions increases with age and

https://doi.org/10.1038/s41467-025-57632-w

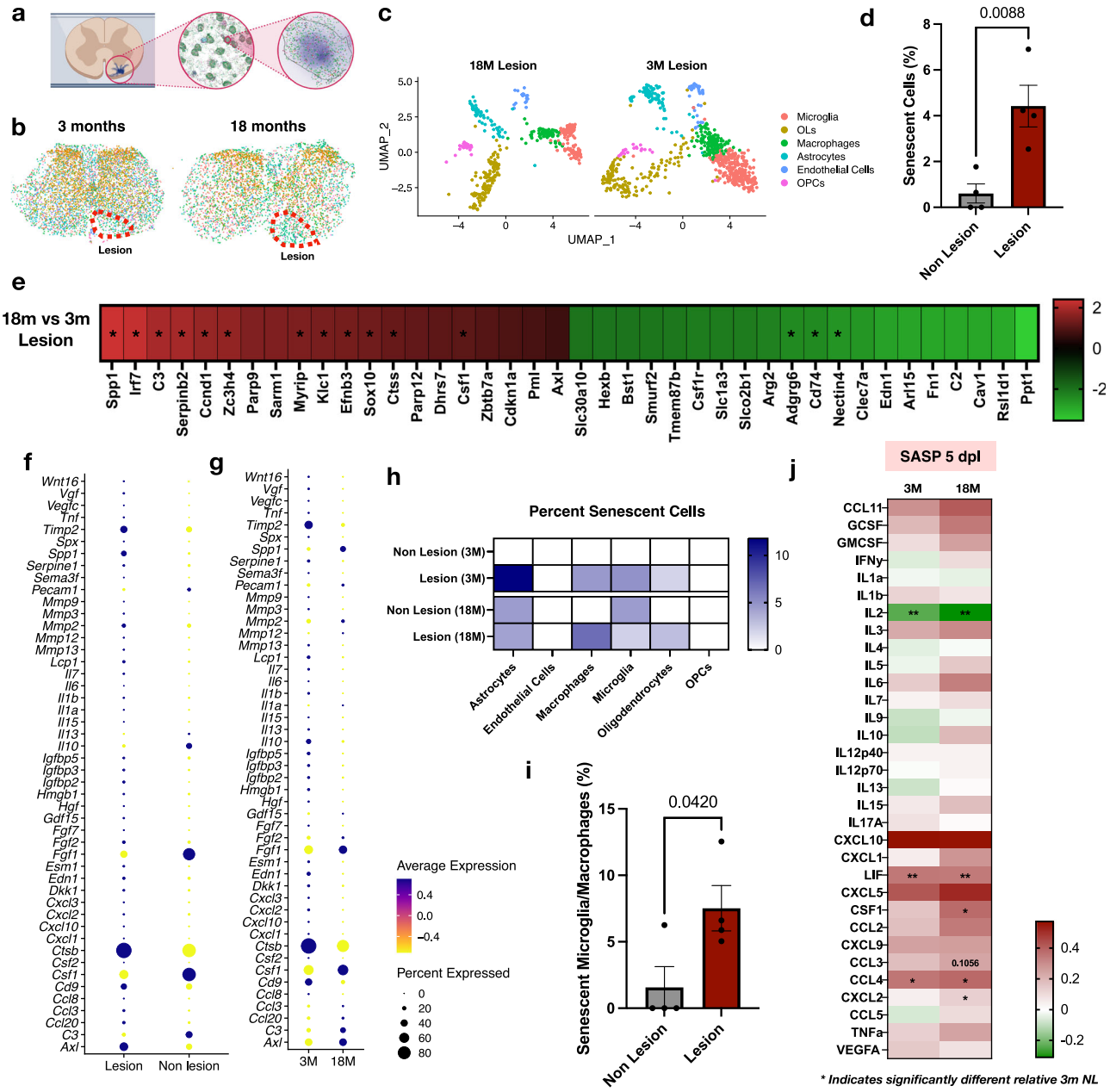

Fig. 2 | Increased senescent markers and SASP proteins characterize aged lesion after demyelination. a Schematic of MERFISH spatial transcriptomics. **b** Demyelinated lesions were traced in young (3 months) and aged (18-22 months) mice at 5 dpl. **c** UMAP visualization of lesion cell types in young and aged lesions ($n = 2$ per group). Uniform manifold approximation and projection (UMAP) visualization of young and aged lesions by cell types. **d** Comparison of senescent cells in pooled lesions vs naïve non-lesion controls regardless of age ($n = 4$ per group; each n denotes biologically independent replicate lesion or non-lesion from the same mouse). **e** Heatmap depicting top differentially expressed genes between young and aged lesions at 5 dpl. Color represents LogFC relative to young lesion and * indicates significantly differentially expressed. **f** Dot plot describing senescent gene expression across pooled lesion and non-lesion ($n = 4$ per group). **g** Dot plot describing senescent gene expression across young and aged lesions ($n = 2$ per group). **h** Heatmap depicting percentage of cell types observed to be senescent in young and aged lesion and non-lesion. Color represents % of cells senescent. **i** Comparison of percentage of senescent microglia and macrophages in pooled lesion and non-lesion regardless of age ($n = 4$ per group; each n denotes biologically independent replicate lesion or non-lesion from the same mouse). **j** Heatmap depicting SASP (senescence associated secretory phenotype) protein levels in young and aged lesions relative to young non-lesioned white matter at 5 dpl ($n = 3$ per group). Color represents LogFC relative to young non-lesion and * indicates significantly differentially expressed. Data are mean ± SEM (**d**, **i**). *P*-values derived from two-sided student's t-test (**d**, **i**), two-way ANOVA with FDR corrected multiple comparisons (**j**) or the two-sided Wald test (**e**). Select figures created in BioRender (2025) (**a**) https://BioRender.com/j71l219. Source data are provided as a Source Data file.

potentially contributes to remyelination impairment. To assess the level of cellular senescence in lesions of aged mice compared to young mice, we performed spatial gene expression profiling of lesioned spinal cord tissues in 3 months (young) and 18-22 months old (aged) mice at 5 days post lesion (dpl) using Multiplexed Error-Robust Fluorescence In Situ Hybridization (MERFISH) with a customized panel designed to characterize senescence associated gene expression (Fig. 2a). The library consisted of RNA probes targeting 400 genes, including 64 genes for cell type identification, 288 genes associated with cellular senescence in prior transcriptomic studies[32,37–39], and 48 genes identified to label microglia subsets associated with disease[40,41] (Supplementary data 1). Focal lesion was delineated by the

hypernuclear DAPI staining in both the young and aged mouse spinal cord sections (Fig. 1a, b and Fig. 2b and Supplementary Fig. 4a). Analysis of distinct cell populations within the outlined lesioned area through UMAP clustering of cell-type associated gene markers revealed all major cell types found in the spinal cord, including microglia, macrophages, OPCs, oligodendrocytes, astrocytes, and endothelial cells (Fig. 2b, c and Supplementary Fig. 4a, b–d). The relative percentage of cells identified in lesions differed substantially from naïve non-lesions. In lesions, an expansion of macrophages and microglia, along with a reduction in oligodendrocytes, was observed at both ages (Supplementary Fig. 4e). Demyelinated lesions from mice of both ages also showed an increase in senescent cells compared to naïve non-lesioned tissue (Fig. 2d). Moreover, demyelinated lesions exhibited a significant increase in transcripts associated with senescence, such as *Lgals3*[42,43], *Spp1*, and *Ctsb*, compared to naive tissues (Fig. 2f and Supplementary Fig. 4f). When comparing lesions between aged and young mice, we found that lesions from aged mice exhibited an upregulation of genes associated with cellular senescence and microglial activation, including *Spp1* and *C3*, both part of the SenMayo and DAM genesets, *Irf7*, which has been shown to induce senescence[44], *Ccnd1*, which is hyper-expressed in SCs[45], and *Efnb3*, which is necessary for SC survival[46] (Fig. 2e, g). Interestingly, distinct senescent markers were differentially expressed in the young and aged mouse lesions at 5 dpl, suggesting potential alterations in temporal dynamics of senescent cell responses associated with age (Fig. 2g). Additionally, we identified multiple cell types within lesions expressing varying levels of senescence-associated transcripts (Supplementary Fig. 4g). Astrocytes constituted the largest proportion of senescent cells in young mouse lesions, but their activity is reduced in aged mouse lesions (Fig. 2h). By contrast, macrophages increased and predominated in aged lesions. Notably, there was a significant increase in the percentage of microglia and macrophages exhibiting senescent gene expression in lesions compared to naïve, non-lesioned tissue (Fig. 2i), consistent with our findings in Fig. 1. Moreover, oligodendrocytes in lesions exhibit low levels of senescence activity at both ages. These results suggest age influences senescence activity in cell populations differently within lesions.

To examine the presence of senescence associated secretory phenotype (SASP) factors in lesions, we performed multiplex protein analysis of dissected lesions and naive tissues at 5 dpl in 3 months old and 18 months old mice. In both age groups, we found that lesioned tissues exhibited a decrease in IL2, an increase in LIF, and an increase in CCL4 compared to naive control tissues (Fig. 2j). Moreover, in 18 months old lesions, an increase in CSF1, CXCL2, and IL5 was observed compared to 3 months old lesions (Supplementary Fig. 4h–j). Taken together, these data indicate that at 5 dpl, aged mice exhibit increased cellular senescence accompanied by an elevation in SASP factors in demyelinated lesions compared to young mice.

To determine whether the presence of SCs in lesions is associated with inefficient remyelination in aged mice, we compared P21 expression in lesions of 3 months old and 18 months old mice. We observed that 18 months old (aged) mice exhibited increased P21 expression compared to 3 months old (young) mice at 20 dpl (Supplementary Fig. 5a, b), with this increase persisting at 60 dpl (Supplementary Fig. 5c, d). Similarly, we observed increased p16tdt+ staining in 12 months old (middle-aged) lesions compared to 3 months old (young) lesions at 10 dpl (Fig. 3a, b), but no difference between ages at 5 dpl (Fig. 3c, d). Furthermore, p16tdt expression was negligible for both ages in naïve tissue (Supplementary Fig. 5e) These results suggest a potential difference in temporal dynamics of senescence activity in the lesions with age. The sustained elevation of P21 in mice at 18 months old mice coincided with a reduction in OPC differentiation and mature oligodendrocytes within the lesion at 20 dpl (Fig. 3e–h and Supplementary Fig. 5f). While prior studies have reported no change in initial demyelinating lesion sizes between ages[47–49], we found a slight, but significant, increase in lesion cross-sectional area in 18 months old mice at 20 dpl (Supplementary Fig. 5g).

To further characterize the difference in senescence-associated activities in lesions between young and aged mice, we performed bulk-RNA sequencing of 20 dpl lesions from mice at 3 months and 18 months old (Fig. 3i). We identified 434 differentially expressed genes between the lesions of young and aged mice (Fig. 3j). Using the SenMayo gene panel, we identified 14 senescence associated transcripts that were significantly differentially expressed in lesions of 18 months old mice compared to 3 months old mice (Fig. 3k). Moreover, transcripts corresponding to damage associated microglia (DAM) were also elevated in 18 months old mice compared to 3 months old mice (Supplementary Fig. 5h). Immunostaining analysis of IBA1 and CD68 for activated microglia confirmed 18 months old mice exhibited elevated microglial activation in lesions at 20 dpl compared to 3 months old mice, but their levels were found to decrease to similar levels as 3 months old mice by 60 dpl (Supplementary Fig. 5i–l). We also examined the levels of SASPs in the lesions at 20 dpl and found that 18 months old mice exhibited increases in CSF1, CCL4, CCL5, CCL11, CXCL1, CXCL2, and a decrease in IL2 compared 3 months old mice (Fig. 3l). These findings indicate that demyelinated lesions of aged mice exhibit prolonged SC and DAM activity compared to young mice, corresponding with the failure of OPCs to efficiently differentiate into mature remyelinating oligodendrocytes.

Senolytic treatment increases remyelination in an age-dependent manner

To examine the effect of SC reduction on remyelination efficiency, we performed LPC-induced demyelination on INK-ATTAC (IA) mice. These mice are genetically engineered to express a fusion protein of FK-binding protein and caspase-8 under the control of the *P16*^{ink4a} promotor, allowing selective apoptosis of p16-expressing SCs upon systemic administration of the synthetic drug AP20187 (AP)[19] (Fig. 4a). LPC-induced demyelination was performed on 3 months old IA mice followed by treatment with either AP (2 mg/kg) or vehicle (control) twice a week until 20 dpl before they were perfused for immunostaining analysis (Fig. 4b). We found that mice treated with AP exhibited an increase in Olig2+ oligodendrocyte lineage cells and a corresponding increase in CC1+ mature oligodendrocytes within lesions compared to control (Fig. 4d–f and Supplementary Fig. 6a). Moreover, scanning electron microscopy (SEM) analysis of lesions revealed AP treatment led to a modest, but significant increase in remyelination compared to vehicle treated control (Fig. 4g, h and Supplementary Fig. 6b).

To determine whether the pro-regenerative effects of AP on young IA mice are driven by its impact on SC cell activity during early or late stages of remyelination, 3 month old IA mice were treated with AP or vehicle twice weekly from the day of lesion induction to 10 dpl, or from 10 dpl until 20 dpl (Supplementary Fig. 6c). Immunostaining analysis revealed AP treatment from days 1-10 dpl did not influence oligodendrocyte lineage cells progression compared to vehicle treated mice. However, AP treatment from days 10–20 significantly increased the number of oligodendrocyte lineage cells and mature oligodendrocytes compared to vehicle-treated mice, similar to the effects observed with AP treatment throughout the entire remyelination period (Supplementary Fig. 6d–g). These results suggest that AP treatment may facilitate the clearance of senescent cells and modulate the inflammatory environment.

To determine whether the reduction of senescent cells (SCs) can enhance remyelination in older mice, LPC-induced demyelination was performed in 12-month-old (middle-aged) and 18–22-month-old (aged) IA mice, followed by treatment with AP or vehicle. In 12-month-old mice, AP treatment produced a significant pro-remyelinating effect, as indicated by increased MBP staining (Fig. 4i–l and Supplementary Fig. 7a, d). However, unlike in 3-month-old mice, the density of

https://doi.org/10.1038/s41467-025-57632-w

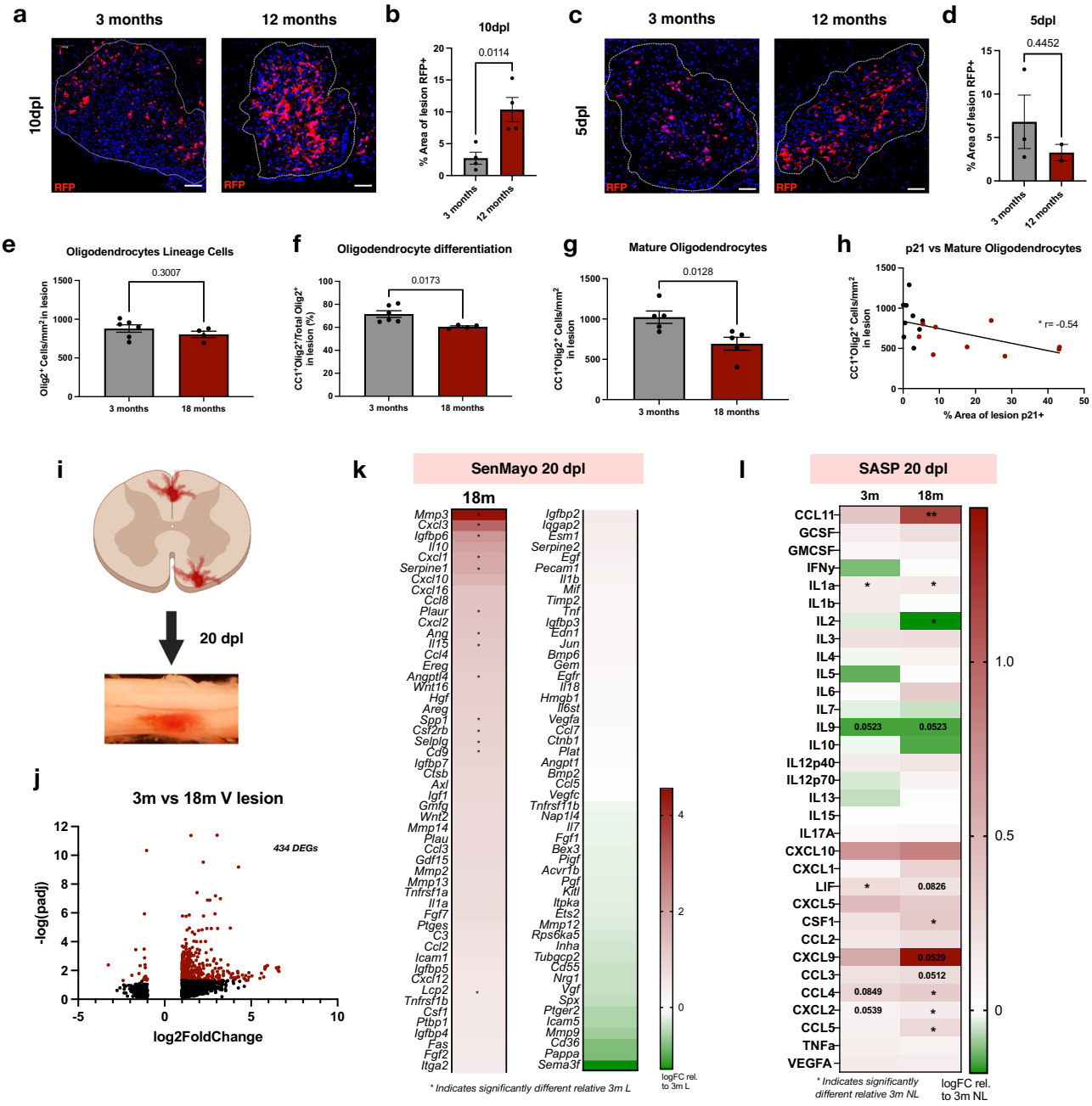

Fig. 3 | Persistence of senescent cells in lesions are associated with impaired oligodendrocyte differentiation in aged mice. a Immunofluorescent staining of p16tdt in young (3 months) and middle-aged (12 months) lesions at 10 dpl (days post lesion). **b** Quantification of p16tdt+ cells in a ($n = 4$ per age). **c** Immunofluorescent staining of p16tdt in young and middle-aged lesions at 5 dpl. **d** Quantification of p16tdt+ cells in (**c**) ($n = 3$ 3 m, 2 18 m). **e** Quantification of OLIG2 in young and aged (18–22 months) lesions ($n = 6$ 3 m, 4 18 m). **f** Quantification of percentage of differentiated oligodendrocytes in young and aged lesions ($n = 6$ 3 m, 4 18 m). **g** Quantification of mature oligodendrocytes with CC1 and OLIG2 in young and aged lesions (n = 5 per age). **h** Correlation between P21+ staining and mature oligodendrocytes (CC1 + OLIG2 +) in the lesions. **i** Experimental schematic of lesion microdissection and neutral red for bulk RNA-sequencing. **j** Volcano plot of significantly differentially expressed genes between young lesions and aged lesions at 20 dpl ($n = 3$ per group). Genes with adjusted p-values < 0.05 and absolute log2 fold changes >1 were called as differentially expressed genes for each comparison. **k** Heatmap depicting SenMayo gene expression in aged lesions relative to young lesions (n = 3 per group). Color represents LogFC relative to young lesion and * indicates significantly differentially expressed. **l** Heatmap depicting SASP (senescence associated secretory phenotype) protein levels in young and aged lesions relative to young naïve non-lesioned white matter ($n = 3$ per group). Color represents LogFC relative to young naïve non-lesion and * indicates significantly differentially expressed. Data are mean ± SEM (**b**, **d**–**g**). Scale bar, 50 μm (**a**, **c**). *P* values derived from two-tailed unpaired Student's t-tests (**b**, **d**–**g**), simple-linear regression (**h**), two-way ANOVA with FDR corrected multiple comparisons (**l**) or the two-sided Wald test (**j**, **k**). Select figures created in BioRender (2025) (**i**) https://BioRender.com/r92t091Source data are provided as a Source Data file.

oligodendrocyte lineage cells within the lesions remained unchanged (Fig. 4j). In contrast, AP treatment in 18-month-old aged mice did not influence the density of oligodendrocyte lineage cells, the percentage of mature oligodendrocytes, or MBP levels in lesions compared to vehicle-treated controls (Fig. 4m–p and Supplementary Fig. 7b, e). These findings suggest that senolytic treatment facilitates oligodendrocyte maturation and remyelination in young and middle-aged mice but fails to exert similar effects in aged mice.

To translate our findings to a more clinically relevant model, we performed similar experiments in a cohort of 12-month-old mice by

https://doi.org/10.1038/s41467-025-57632-w

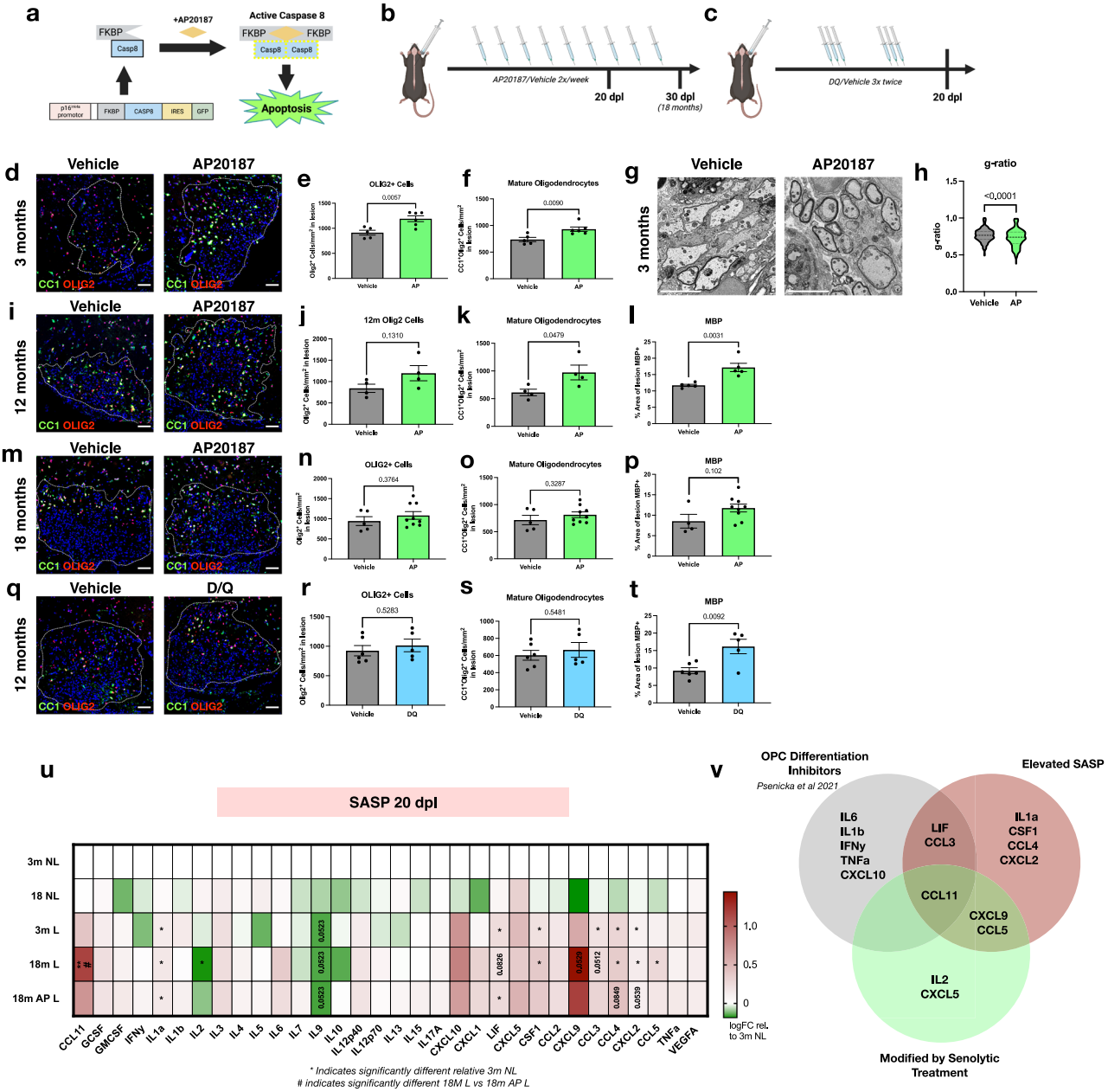

Fig. 4 | Treatment with senolytics increases remyelination in young but not aged mice. a Schematic of INK-ATTAC mouse model. **b**, **c** Experimental schematics of vehicle, AP20187 (2 mg/kg) and Dasatinib (5 mg/kg)/ Quercetin (50 mg/kg) (D/Q) treatments. **d**, **i**, **m**, **q** Immunofluorescent staining of mature oligodendrocytes and oligodendrocyte lineage cells with CC1 and OLIG2 in (**d**) young (3 months) vehicle and AP treated lesions at 20 dpl (days post lesion), **i** middle-aged (12 months) vehicle and AP treated lesions at 20 dpl, (**m**) aged (18–22 months) vehicle and AP treated lesions at 30 dpl, and (**q**) middle-aged (12 months) vehicle and D/Q treated lesions at 20 dpl. **e**, **f** Quantification of OLIG2+ and CC1 + OLIG2+ cells in (**d**) ($n = 5$ V, 6 AP). **g** Scanning electron microscopy images of remyelinated axons in young vehicle and AP treated lesions at 20 dpl ($n = 3$ mice per group). **h** Violin plot of g-ratio's of remyelinated axons counted from g ($n = 300–400$ axons per group). **j**–**l** Quantification of OLIG2+ and CC1 + OLIG2+ cells and MBP+ area in i and extended fig. 7a ($n = 4$ per group (**j**–**k**); $n = 5$ per group i). **n**–**p** Quantification of OLIG2+ and CC1 + OLIG2+ cells and MBP+ area in m and extended fig. 7b ($n = 5$ V **n**–**o**, 4 V **p**, $n = 9$ AP **n**–**p**). **r**–**t** Quantification of OLIG2+ and CC1 + OLIG2+ cells and MBP+ area in (**q**) and extended fig. 7c ($n = 6$ V, 5 D/Q). **u** Heatmap depicting SASP (senescence associated secretory phenotype) protein levels in young naïve non-lesion, aged non-lesion, young vehicle treated, aged vehicle treated, and aged AP treated lesions relative to young naïve non-lesioned white matter ($n = 3$ per group). Color represents LogFC relative to young non-lesion and * indicates significantly differentially expressed from 3 m non-lesion, # indicates significantly differentially expressed between 18 mL and 18 m AP L. **v** Venn-diagram of elevated SASP factors in the aged demyelinated lesions, SASP factors changed with AP treatment, and proteins known to restrict OPC differentiation. Data are mean ± SEM (**e**, **f**, **h**, **j**–**l**, **n**–**p**, **r**–**t**). Scale bar, 50 μm (**d**, **i**, **m**, **q**), 2 μm (**g**). *P*-values derived from two-tailed unpaired Student's t-tests (**e**, **f**, **h**, **j**–**l**, **n**–**p**, **r**–**t**), or two-way ANOVA with FDR corrected multiple comparisons (**u**). Select figures created in BioRender (2025) (**a**) https://BioRender.com/p01d544, **b**, **c** https://BioRender.com/x25z952. Source data are provided as a Source Data file.

administering the senolytic cocktail of dasatinib and quercetin (D/Q). D/Q is currently being used in several clinical trials to deplete senescent cells[46,50], and our reanalyzed snRNA-sequencing data[31] shows increased myeloid cell expression in the lesion of many of the anti-apoptotic genes D/Q targets (Supplementary Fig. 7g). Similar to AP treatment, we found a two week regiment of D/Q treatment (Fig. 4c) resulted in a pro-myelinating effect as indicated by increased MBP staining (Fig. 4q–t and Supplementary Fig. 7c, f).

We next sought to determine the mechanism by which senolytic treatment enhances remyelination in young and middle-aged mice but not in aged mice. To compare SC activities in lesions between young and aged mice after AP treatment, we conducted bulk RNAseq analysis of lesioned tissues from 3 months old and 18 months old mice at 20 dpl. Aged lesions with and without treatment were compared to young non-lesion and lesion due to their prolonged remyelination period and amplified senescence phenotype, where gene and protein differences would be more readily captured. We identified 434 differentially expressed genes between 3 months old and 18 months old mouse lesions following vehicle treatment (Fig. 3j), compared to only 70 differentially expressed genes after AP treatment (Supplementary Fig. 8a). Additionally, no differential expression of SenMayo or DAM genes was observed in AP treated 18 months old mouse lesions compared to 3 months old mouse lesions (Supplementary Fig. 8b, c). These results suggest that in contrast to lesions in aged mice, which exhibit sustained upregulation of senescence and DAM associated transcripts at 20 dpl, AP treatment reduces these transcripts to levels similar to those in young mice. We also determined if cellular senescence in lesions is altered at the protein level by measuring the level of SASP proteins in lesions at 20 dpl in 18 months old mice with or without AP treatment. Following AP treatment, we observed a decrease in multiple SASP factors in lesions, including CCL11, CXCL9, and CCL5, and an increase in IL2, which were no longer differentially expressed compared to control naive tissue (Fig. 4u). These findings suggest AP treatment reduces SC activity in aged mouse lesions despite the lack of significant improvement in remyelination. Possible explanations for the failure to increase remyelination in aged mice are that some SASP factors may remain in lesions after AP treatment, thereby preventing oligodendrocyte differentiation, or that treatment with senolytics or SC reduction alone is insufficient to improve remyelination from aged OPCs in an already aged CNS environment that has multiple inhibitory factors to regeneration.

CCL11 is a SASP factor driving remyelination impairment

To identify SASP factors that may contribute to remyelination impairment in aged mice, we compared SASP factors elevated in aged lesions with those modified by AP-treatment. This narrowed our search to CCL5, CCL11, and CXCL9. When these factors were cross-referenced against proteins known to inhibit OPC differentiation[51], CCL11 emerged as a potential mechanistic target (Fig. 4v). CCL11/Eotaxin1 is a chemokine that selectively recruits eosinophils, is elevated with age in humans and mice[52–54], and has been shown to promote senescence[55]. Recently, it was also shown to interact with the central nervous system in multiple ways: CCL11 efficiently crosses the blood brain barrier[56], has been implicated in neuroinflammatory disorders and SARS-CoV-2 (COVID-19) cognitive impairment[57,58], and impairs neurogenesis[54,58,59]. Moreover, OPCs have been suggested to express the primary CCL11 receptor, CCR3[60] and elevated CCL11 levels are associated with MS disease duration and severity[61,62]. These observations, combined with our findings, suggests CCL11 may play a central role in senescence-associated remyelination delay.

To determine if CCL11 is detected in senescent cells, LPC-induced demyelination was performed on p16tdt mice. We observed co-localization of CCL11 with p16tdt in lesions but not naïve control tissue (Fig. 5a and Supplementary Fig. 9a) and found that CCL11 co-labeled with IBA1+ microglia in lesions of both 3 months old and 18 months old mice (Fig. 5b). Moreover, the expression level of CCL11 was significantly higher in lesions of 18 months old mice compared to 3 months old mice (Fig. 5c) and is relatively absent in naïve control tissue of both ages (Supplementary Fig. 9a). We also analyzed our SASP protein multiplex data of demyelinated lesions at 20 dpl and found that CCL11 was upregulated in the lesions of 18 months old mice compared to those of 3 months old mice (Fig. 5d). Furthermore, AP treatment reduced its expression in 18 months old mouse lesions to levels comparable to 3 months old mice (Fig. 5d). To validate our findings clinically, we also assessed the concentration of CCL11 in the plasma of individuals with MS and healthy controls (Supplementary Fig. 9b). We found a significant association between age and CCL11 concentration across all samples (Supplementary Fig. 9c), and interestingly, the increase in CCL11 concentration with age also paralleled disease progression (Fig. 5e). These results indicate CCL11 level increases with age and MS disease progression, and suggests inhibition of CCL11 may prevent senescence-mediated remyelination failure in MS.

To determine if CCL11 inhibition enhances remyelination efficiency, we administered a CCL11 neutralizing antibody (CCL11na) systemically twice a week during the remyelination phase in 3 months old mice following LPC-induced demyelination (Fig. 5f). At 20 dpl, increased MBP staining was observed in lesions of mice treated with CCL11na compared to the isotype control (Fig. 5g, i). Analysis of LAMP1, a marker for early lysosomes, in lesions at 20 dpl revealed minimal overlap between MBP and LAMP1, indicating that the increase in MBP levels following CCL11na treatment was not due to myelin debris accumulation (Supplementary Fig. 9e, f). However, CCL11na administration did not affect the number of mature oligodendrocytes in the lesions (Fig. 5h, j), suggesting that CCL11 inhibition influences oligodendrocyte maturation and myelination, but not differentiation.

To determine if CCL11 gain-of-function impairs remyelination, we administered recombinant CCL11 (rCCL11) into 3 months old mice twice a week during remyelination following LPC-induced demyelination. We found that rCCL11 administration did not have any detectable effect on remyelination compared to vehicle, suggesting systemic delivery of rCCL11 into mice may not be sufficient to impact remyelination (Fig. 5g–j). To determine if CCL11 can directly influence oligodendrocyte maturation, we next tested the effect of rCCL11 on rat primary oligodendrocyte cultures in vitro. To this end, cultures were treated with recombinant CCL11 (rCCL11) during differentiation from DIV2 to DIV5 (Fig. 5k). At time of fixation (DIV5), we found that all oligodendrocytes expressed O4, a premyelinating marker (Supplementary Fig. 9d), and most oligodendrocytes expressed varying levels of MBP. Therefore, we further segregated cells into those with low MBP expression and those with high MBP expression (Fig. 5l). In the rCCL11-treated group, we observed more cells with low MBP expression (Fig. 5m) and fewer cells with high MBP expression (Fig. 5n). This observation suggests CCL11 inhibits efficient MBP expression in maturing oligodendrocytes in a cell-autonomous manner. Taken together, our results suggest the SASP factor CCL11 contributes to the inhibitory effects of senescent cells on remyelination, and that depletion of CCL11 enhances oligodendrocyte maturation by increasing MBP expression.

Discussion

Aging is the primary risk factor for progression in most neurodegenerative diseases, and with it comes the accumulation of senescent cells. While the role of SCs in these diseases is beginning to be understood, their impact on remyelination in MS is still poorly defined. Here, we report the emergence of senescent microglia and macrophage cells following demyelination, with gradual clearance throughout remyelination. We also find this phenomenon increases with age, which is known to be associated with a reduced capacity to remyelinate. Previous studies have shown the accumulation of SCs occurs in injured or damaged tissue in young and aged animals, often as a stress-induced response[63,64]. These SCs have been found to exhibit beneficial effects for regeneration, and become damaging only if unresolved in a timely manner, such as in the context of aging[65]. Other studies have shown contradictory evidence where this SC response limits regeneration throughout repair and regenerative processes and offers no benefits irrespective of age[66,67]. While the beneficial or detrimental effects of damage-induced SCs are likely cell-type and context dependent, we

https://doi.org/10.1038/s41467-025-57632-w

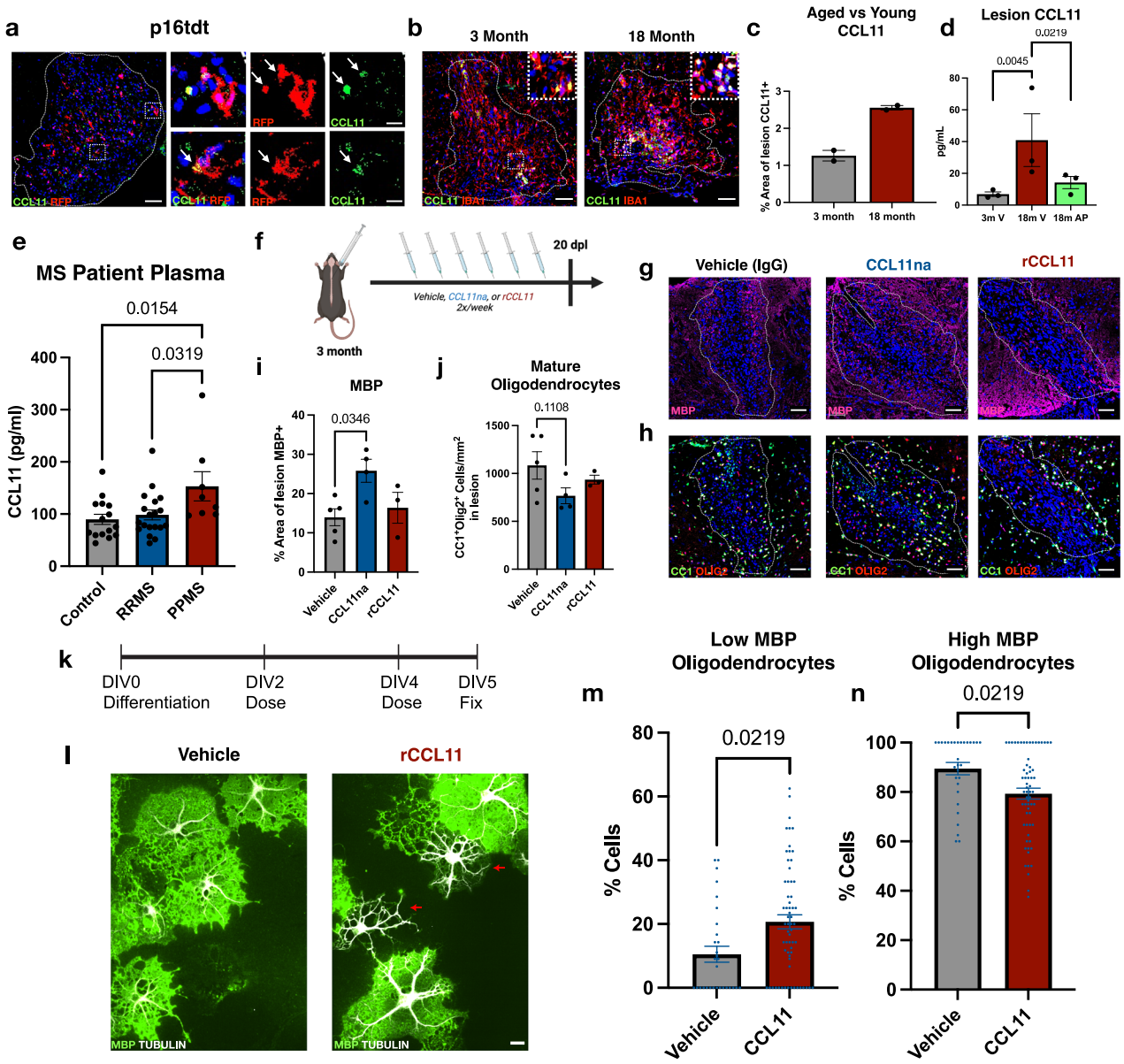

Fig. 5 | CCL11 is a SASP factor driving remyelination impairment. **a** Immunofluorescent staining of p16tdt+ cells (RFP) and CCL11 in 12 months old demyelinated lesions. Arrows indicate p16tdt + CCL11+ colocalization ($n = 4$ mice). **b** Immunofluorescent staining of microglia (IBA1) and CCL11 in young (3 months) and aged (18–22 months) demyelinated lesions. **c** Quantification of CCL11 in **b** ($n = 2$ per group). **d** Protein levels of CCL11 in young, aged vehicle treated, and aged AP treated lesions at 20 dpl ($n = 3$ per group; each n denotes biologically independent replicate). **e** CCL11 plasma concentrations in healthy control, Relapse Remitting MS, and Primary Progressive MS samples (n = 15 C, 19 RRMS, 8 PPMS, uncorrected for age; each n denotes biologically independent replicate). **f** Experimental schematic of IgG vehicle (50 μg/kg), CCL11 neutralizing antibody (CCL11na) (50 μg/kg), or recombinant CCL11 (rCCL11) (10 μg/kg) treatment of young lesions. **g**, **h** Immunofluorescent staining of mature oligodendrocytes with CC1 and OLIG2 and myelin with MBP in vehicle, CCL11na, and rCCL11 treated lesions at 20 dpl. **i**, **j** Quantification of MBP+ area and CC1 + OLIG2+ cells in (**g**, **h**) ($n = 5$ V, 4 CCL11na, 3 rCCL11; each n denotes biologically independent replicate). **k** Schematic of in vitro experiment timeline. **l** Immunofluorescent staining of primary rat oligodendrocytes treated with vehicle or recombinant CCL11 (100 ng/μL dosed at DIV2, DIV4) for MBP and alpha/beta tubulin. Red arrows denote low MBP cells. **m** Quantification of DIV5 oligodendrocytes demonstrate higher percentage of CCL11-treated cells have low MBP expression (20.7 ± 2.2%) compared to control cells (10.5 ± 2.5%) **n**, Quantification of DIV5 oligodendrocytes demonstrate lower percentage of CCL11-treated cells have high MBP expression (79.3 ± 2.2%) compared to control cells (89.5 ± 2.5%) (for **m**, **n**: $n = 30$ FOVs for control group and $n = 63$ FOVs for rCCL11-treated group across cultures from 2 biological replicates, 3 experiments, 1–2 coverslips per condition per experiment. Data points refer to fields of view). Images represent half field of view. Data are mean ± SEM (**c**–**e**, **i**, **j**, **m**, **n**). Scale bar, 50 μm (**a**, **b**, **g**, **h**), 20 μm (**i**), 10 μm (**a**, **b** insets). *P*-values derived from two-sided Kolmogorov-Smirnov t-test (**m**, **n**), one-way ANOVA with Tukey corrected multiple comparisons (**d**, **i**, **j**), or one-way ANOVA with FDR corrected multiple comparisons (**e**). Select figures created in BioRender (2025) (**f**) https://BioRender.com/x25z952. Source data are provided as a Source Data file.

show here that in the context of remyelination, senescent microglia and macrophages limit remyelination. In an age dependent manner, we observe an increased and prolonged senescence response to demyelination, possibly due to the failure of the aged microglia to clear the SCs as efficiently[68]. Treatment with genetic and pharmacologic senolytic methods resulted in increased numbers of mature oligodendrocytes and improved remyelination in lesions of young and middle-aged mice. Despite multiple attempts to verify reduction of

senescent cells, we were unable to confirm the efficacy of the treatments in clearing senescent cells. This may be due to the well-known unreliability of common senescent marker antibodies (P16, P21, B-galactosidase)[32].

We also showed that multiple SASP factors are dysregulated in aged mouse lesions and were returned to younger levels with treatment of senolytics. In particular, we found that CCL11/Eotaxin-1 is one of the most drastically altered SASP proteins following senolytic treatment. CCL11 has previously been shown to be associated with aging[52,54] and MS disease severity[61,62], and to impair neurogenesis and myelination[54,58,59], Moreover, CCL11 has been shown to cause cognitive dysfunction in neuroinflammatory disorders and SARS-CoV-2 (COVID-19)[57,58] and to promote senescence[55]. Here, we found treatment with recombinant CCL11 in vitro resulted in reduced MBP production in maturing oligodendrocytes in a cell-autonomous manner. Additionally, following CCL11 inhibition during remyelination in young mice, we observed similar beneficial remyelinating effects as when senescent cells were treated with AP and D/Q. However, we did not see an effect of artificially raising the levels of CCL11 with recombinant protein. This could be due to CCL11 levels potentially being saturated in the lesion environment or due to treating with rCCL11 systemically and not locally, as was necessary in Villeda et al. 2021[54]. Interestingly, an elevation of plasma CCL11 level was observed in MS patients with age, concurrent with disease progression. While future studies will need to be conducted to determine whether CCL11+ myeloid cells are present in patient lesions, evidence suggests microglia are the primary cell-type in the CNS responsive to CCL11[58]. Together, since MS exhibits features of increased aging, it is possible that elevated levels of SCs with chronic disease result in increased SASP including CCL11, which inhibit remyelination and promote the deterioration of symptoms.

However, we found that treatment with senolytics did not significantly improve remyelination in aged mice, despite modifying the lesion environment. This limited effect may be due to incomplete clearance of SCs or lingering SASP production in the aged lesions. Indeed, AP treatment modified SASP profiles within the aged lesions but several factors remained elevated (Fig. 4u). Additionally, it is likely that the presence of SCs is only one of multiple factors limiting remyelination in the aged nervous system. Other factors known to change with age include increased chronic inflammation[69], modified niche stiffness[70], and inefficient myelin debris removal and processing by microglia and macrophages[71]. Similarly, changes in OPCs with age result in reduced recruitment[72] and limited intrinsic capacity to differentiate[71,73]. Analogously, we found differing proportions of cell types showing features of senescence with age (Fig. 2h). In young lesions at 5 dpl, astrocytes and myeloid cells showed the highest percentage of senescent cells, while in aged lesions myeloid cells increased their percentages. The small sample sizes for these transcriptomic experiments limit the scope of conclusions that can be inferred and further studies with larger sample sizes and conditions will be needed to fully characterize these age-induced differences in cell-populations throughout remyelination and could explain the differences in efficacy of senolytic treatment on remyelination.

The cause of senescent microglia accumulation following demyelination has yet to be established. Studies have shown substantial overlap between senescent cells and inflammatory macrophages[74,75], but where the demarcation between inflammatory cells and senescent cells lies is currently unclear. With this in mind, here we utilized multiple complementary methods to characterize and confirm a senescence phenotype following demyelination, in line with recently released guidance for studying senescence[76]. Recent reports also suggest substantial overlap in transcriptional profiles between disease associated microglia (DAM), white matter associated microglia (WAM), and senescent cells[43,77,78], all of which have been reported in various models of demyelination[79–81]. While the relationship between these phenotypes remains unclear, recent studies suggest DAM are highly proliferative before becoming senescent[77] and that inhibiting microglial proliferation limits DAM and senescent microglia accumulation[37]. Indeed, we found that almost all commonly associated DAM genes were upregulated in young lesions at 20 dpl compared to naive control white matter (Supplementary Fig. 9g). Together, it is conceivable that in response to myelin damage, microglia proliferate and enter the DAM/WAM activation state to process the debris. However, a subset of microglia may proliferate too vigorously, leading to the accumulation of replication stress[82] and the triggering of senescence programming. While SCs are effectively cleared from demyelinated lesions in young mice, resulting in a transient phenomenon, the aged immune system may be less adept, leading to inefficient remyelination. It is likely that this response is not specific to demyelination, but injury-induced senescence in general, while myelin debris exacerbates this phenotype in the context of MS. Future studies will be needed to delineate the effects of sham injury-induced senescence compared to demyelination-induced senescence.

In conclusion, this study provides an important step to understand how demyelination promotes the accumulation of senescent cells in lesions, and how especially with age, these cells limit remyelination through SASP production. Future studies are still needed to elucidate the exact contributions of individual lingering SASP factors on remyelination with age. Our study suggests treatment with senolytics alone may not be sufficient to enhance remyelination with age, and that inhibiting lingering SASP activity, such as CCL11, may be a better strategy to improving the lesion environment for remyelination. This approach may have therapeutic potential for reversing the aging lesion environment and enhancing the remyelination process in MS.

Methods

Study approval

All animal experiments were conducted in compliance with relevant ethical regulations and guidelines. The study protocol (2016-1123) was approved by the Institutional Animal Care and Use Committee at Georgetown University.

Mice

All transgenic mice were maintained on a C57BL/6 background. Heterozygous p16-tdTomato mice (B6J.Cg-*Cdkn2a*^{tm4Nesh}/Mmnc) were obtained through the NIH Mutant Mouse Resource & Research Center[30]. INK-ATTAC mice were obtained from Unity Biotechnology. C57BL/6 mice were purchased from Jackson Labs (strain 000664). Mice were kept in home-cages at 22 ± 2 C (50% humidity) and maintained on a 12 h-light/12-hour-dark cycle with food and water ad libitum until the comparable human age of young adult (2–3 months), middle aged (12 months), or aged adult (18–22 months). Euthanasia was administered with 3% isoflurane followed by perfusion and cervical dislocation. Mice of both sexes were used for all experiments. Despite MS predominantly occurring in females, we did not have statistical power to differentiate the effects of sex.

Focal Demyelination

Focal demyelinating lesions were induced as previously described in ref. 28. In brief, 1 µL of 1% L-α-Lysophosphatidylcholine (LPC, MilliporeSigma #L4129) in PBS was injected via pulled glass needle attached to a Hamilton syringe between the T11-T12 vertebrae into the ventral white matter columns of the mouse spinal cord. Remyelination was measured at 20 dpl, except where noted in 18–22 month mouse experiments at 30 dpl and 60 dpl.

Treatments

AP20187. INK-ATTAC mice were treated twice a week intraperitoneally with AP20187 (2 mg/kg, MedchemExpress B/B homodimerizer, #HY-13992) or with vehicle (10% DMSO, 40% peg400, 5% tween 80, 45%

saline) at equal volumes (10 µL/g bodyweight) from day of lesion until final timepoint.

Dasatinib/Quercetin. 12 month old C57BL/6 mice were treated three consecutive days twice, one week apart, via oral gavage with dasatinib monohydrate (5 mg/kg, ThermoFischer 462320010) and quercetin hydrate (50 mg/kg, ThermoFischer 174070100) or vehicle (10% etoh, 30% peg400, 60% phosphal 50 PG) at equal volumes (5 µL/g bodyweight) starting on day 8 post lesion.

CCL11 neutralizing antibody. 12 week old INK-ATTAC mice were treated twice a week intraperitoneally with CCL11 neutralizing antibody (50 µg/kg, R&D Systems #MAB420-100), control rat IgG2a isotype (50 µg/kg, R&D Systems #MAB006), or recombinant CCL11 (10 µg/kg, R&D Systems #420-ME-020/CF) at equal volumes (10 µL/g bodyweight) from day of lesion until final timepoint.

In Vivo Imaging System (IVIS)

At 5 dpl, p16-tdtom lesioned, p16-tdtom sham lesioned, and C57BL/6 wild-type control lesioned mice were anesthetized and bioluminescence was imaged using the IVIS Lumina III In Vivo Imaging System.

Real Time qPCR

To identify and dissect out the lesion, 500 µL 1% neutral red dye in PBS was injected intraperitoneally 2 h prior to cardiac perfusion with ice cold 1X PBS[28]. RNA was isolated using the Direct-zol RNA Miniprep Kits (Zymo Research #R2050) and reverse transcribed to cDNA using the iScript gDNA Clear cDNA Synthesis Kit (Biorad #1725034). RT-qPCR was performed with SsoAdvanced Universal SYBR Green Supermix (Biorad #1725271). Primers used were purchased from Bio-Rad: *Rpl13a* (qMmuCED0040629), *Cdkn2a* (qMmuCED0038108), *Rb1* (qMmuCID0005286), *Tert* (qMmuCID0018719), *Apoe* (qMmuCED0044813), *Trem2* (qMmuCID0020213), *Cdkn1a* (qMmuCED0025027), *E2f1* (qMmuCID0005113), *Trp53* (qMmuCID0006264). Expression levels were expressed using the $2^{-\Delta\Delta Ct}$ method normalized to non-lesion tissue.

Immunohistochemistry

Mice were cardiac perfused with ice cold 4% paraformaldehyde in PBS and dissected spinal cords were post fixed overnight at 4 °C, followed by 30% sucrose (w/v) in PBS overnight at 4 °C, before being embedded and frozen in Tissue-Tek O.C.T. compound (Sakura). Lesions were sectioned on a Leica CM1860 cryostat at 12 um. For staining, slides were thawed and dried for 1 h at room temperature (RT) prior to being subsequently washed in TBST (1X TBS, 0.05% Tween), TBS, and permeabilization buffer (1X TBS, 1% Triton X-100). Slides were then blocked for 1 h at RT in blocking/antibody buffer (5% Donkey serum, 1% BSA, 0.4% Triton X) before being stained overnight at 4 °C with the following primary antibodies: mouse anti-APC (CC1) (Abcam #ab16794, 1:100), goat anti-CCL11 (R&D Systems #AF-420-SP, 1:50), rat anti-Cd11b (Biorad #MCA74G, 1:100), CD68 (Biolegend #137020, 1:100), rat anti-Clec7a (InvivoGen #mabg-mdect, 1:100), mouse anti-GFAP (Millipore Sigma #G3893, 1:500), rabbit anti-Iba1 (Fujifilm Wako #019-19741, 1:400), mouse anti-iNos (BD Biosciences #610329, 1:100), mouse anti-LAMP1 (Santa Cruz #sc-20011, 1:100), rat anti-MBP (Biorad #MCA409S, 1:500), mouse anti-Nkx2.2 (DSHB #74.5A5-c, 1:100), rabbit anti-Olig2 (Millipore Sigma #AB9610, 1:300), mouse anti-p16 (Abcam #ab54210, 1:500), mouse anti-p21 (Santa Cruz #sc6246, 1:500), rabbit anti-RFP (Rockland Immunochemicals #600-401-379, 1:1000), rat anti-Sall1 (Invitrogen #14-9729-82). Slides were then washed subsequently in TBST and TBS before being incubated for 1 h in the dark at RT with the following fluorescent conjugated secondary antibodies: Alexa Fluor 488 (Invitrogen, 1:1000), Alexa Fluor 594 (Invitrogen, 1:500) or Cy3 (Jackson ImmunoResearch, 1:500), Cy5 (Jackson ImmunoResearch, 1:500) and Hoechst 33342 (Invitrogen, 1:20,000). Following incubation, the slides were washed again in TBST and TBS before being rinsed with ddH_2O, dried, and mounted with Fluoromount-G mounting medium (Southern Biotech # 0100-01).

For CC1, Olig2, Nxk2.2, LAMP1, Sall1, and CCL11 staining, antigen retrieval was performed prior to staining by incubating the slides in boiling Antigen Retrieval solution (Vector #H-3301-250) for 30 min. For MBP staining, slides were incubated in pre-cooled methanol for 10 min prior to blocking.

Imaging and quantification

Slides were imaged using a Zeiss LSM 800 confocal microscope. Samples were blinded by cage number and ear-tag where applicable. For each sample, 3 lesion sections and 1 non-lesion section were imaged. For analysis, lesions were identified using the DAPI channel and tracing the hyper-nucleated region of the white matter. Percent areas were calculated in FIJI (ImageJ) for each image as follows: background was subtracted, each channel was thresholded to predetermined values based on the channel and experiment, and "% area" of region of interest (pre-traced lesions) was measured. Cells were counted in FIJI (ImageJ) using the "cell counter" plugin and then counts per mm^2 were calculated. 3D reconstruction analysis was done using Imaris microscopy image analysis software (Oxford Instruments).

Scanning electron microscopy and g-ratio

To identify and dissect out the lesion in a mouse spinal cord, 500 µL 1% neutral red dye in PBS was injected intraperitoneally 2 h prior to cardiac perfusion with ice cold fixation buffer (2.5% glutaraldehyde, 1% paraformaldehyde, in 0.2 M sodium cacodylate buffer (Electron Microscopy Sciences). Lesion tissues were then dissected out and cut into 2 mm x 2 mm sections, washed with cold cacodylate buffer (2 mM calcium chloride), and then incubated in osmium solution for 1 h on ice. Tissues were then washed with ddH_2O, incubated with 1% thiocarbohydrazide (TCH) solution (Ted Pella) for 20 min at RT, washed again with ddH_2O, incubated with 2% osmium tetroxide for 30 min at RT, washed with ddH_2O, and then incubated with 1% uranyl acetate at 4 °C overnight. Next, lesioned tissues were then washed with ddH_2O and incubated in pre-heated lead aspartate solution at 60 °C for 30 min, followed by ddH_2O wash, and dehydration with ice-cold freshly prepared 50%, 70%, 85%, 95%, 100% ethanol solutions, and propylene oxide. The tissues were then embedded in resin and incubated at 60 °C for 48 h.

For image acquisition, ultrathin sections (120 nm) containing spinal cord lesions were mounted in silicon wafers and observed with a Teneo LV FEG scanning electron microscope (FEI, Thermo Fisher Scientific). For optimal results, we used the optiplan mode (high-resolution) equipped with an in-lens T1 detector (Segmented A + B, working distance of 8 mm). Low-magnification images (600X) of the entire spinal cord section were first taken to delineate the lesioned site, and then high magnification tile images with multiple captures of our regions of interest (10,000X) were taken to ensure comprehensive coverage of the demyelinated lesion area using 2 kV and 0.4 current landing voltage. For quantification, 2–3 mice (>300 remyelinated axons) from each group were measured for axon diameters and g-ratios (axon diameter/myelin diameter) using MyelTracer (v1.3.1)[83].

SASP Multiplex

To identify and dissect out the lesion, 500 µL 1% neutral red dye in PBS was injected intraperitoneally 2 h prior to cardiac perfusion with ice cold 1X PBS[28]. Spinal cords were extracted and lesion and distant contralateral non-lesion tissue were microdissected out and flash frozen on dry ice. Tissue was homogenized using RIPA buffer with 1% protease inhibitor (Millipore Sigma #P8340) and handheld homogenizer (Fisher Scientific #12-141-361). Following centrifugation, supernatant was moved to new tube and concentrations were

determined via Bradford assay. 100 µL from each sample was then normalized to contain the same amount of protein before being frozen and sent for bead-based multiplex analysis (Eve Technologies, 32-Plex Discovery Assay #MD32).

Bulk RNA sequencing

To identify and dissect out the lesion, 500 µL 1% neutral red dye in PBS was injected intraperitoneally 2 h prior to cardiac perfusion with ice cold 1X PBS[28]. Spinal cords were extracted and lesion and distant contralateral non-lesion tissue were microdissected out and flash frozen on dry ice. RNA was isolated using the Direct-zol RNA Miniprep Kits (Zymo Research #R2050) and sent to Azenta Life Sciences (South Plainfield, NJ, USA) for RNA quality check, library preparation, sequencing and analysis. RNA samples were quantified using Qubit 3.0 Fluorometer (Life Technologies, Carlsbad, CA, USA) and RNA integrity was checked using Agilent TapeStation 4200 (Agilent Technologies, Palo Alto, CA, USA). ERCC RNA Spike-In Mix kit (ThermoFisher #4456740) was added to normalized total RNA prior to library preparation following manufacturer's protocol. RNA sequencing libraries were prepared using the NEBNext Ultra II RNA Library Prep for Illumina using manufacturer's instructions (NEB, Ipswich, MA, USA). Briefly, mRNAs were initially enriched with Oligod(T) beads. Enriched mRNAs were fragmented for 15 minutes at 94 °C. First strand and second strand cDNA were subsequently synthesized. cDNA fragments were end repaired and adenylated at 3'ends, and universal adapters were ligated to cDNA fragments, followed by index addition and library enrichment by PCR with limited cycles. The sequencing libraries were validated on the Agilent TapeStation (Agilent Technologies, Palo Alto, CA, USA), and quantified by using Qubit 3.0 Fluorometer (Invitrogen, Carlsbad, CA) as well as by quantitative PCR (KAPA Biosystems, Wilmington, MA, USA).

The sequencing libraries were clustered on a lane of a NovaSeq 6000 S4 flowcell. After clustering, the flowcell was loaded on the Illumina instrument according to manufacturer's instructions. The samples were sequenced using a 2x150bp Paired End (PE) configuration. Image analysis and base calling were conducted by the Control software. Raw sequence data (.bcl files) generated the sequencer were converted into fastq files and de- multiplexed using Illumina's bcl2fastq 2.17 software. One mismatch was allowed for index sequence identification. After investigating the quality of the raw data, sequence reads were trimmed to remove adapter sequences. The trimmed reads were mapped to the mouse reference genome GRCm38 available on ENSEMBL using the STAR aligner v.2.5.2b. The STAR aligner is a splice aligner that detects splice junctions and incorporates them to help align the entire read sequences. BAM files were generated as a result of this step. Unique gene hit counts were calculated by using feature Counts from the Subread package v.1.5.2. Only unique reads that fell within exon regions were counted. After extraction of gene hit counts, the gene hit counts table was used for downstream differential expression analysis. Using DESeq2, a comparison of gene expression between the groups of samples was performed. The Wald test was used to generate p-values and Log2 fold changes. Genes with adjusted p-values < 0.05 and absolute log2 fold changes > 1 were called as differentially expressed genes for each comparison.

Multiplexed Error-Robust Fluorescence In Situ Hybridization (MERFISH)

To identify and dissect out the lesion, 500 µL 1% neutral red dye in PBS was injected intraperitoneally 2 hours prior to cardiac perfusion with ice cold RNA-ase free 1X PBS[28]. Spinal cords were flash frozen in isopentane and embedded in OCT on dry ice. For MERFISH processing, Vizgen's fresh frozen tissue sample preparation protocol was followed. Briefly, spinal cord sections were sliced at 10 µm. Tissue slices were mounted on Vizgen's bead-coated functionalized coverslip. Once adhered to the coverslip, the samples were fixed (4% PFA in 1X PBS, 15 min, room temperature) and washed (3x, 5 min, 1X PBS). Then samples were photobleached for 3 h in 70% EtOH (Vizgen's photobleacher) followed by an overnight incubation to permeabilize the tissue. Following permeabilization samples were incubated for 30 min in Formamide Wash Buffer (30% deionized formamide (Sigma, S4117) in 2× SSC (Thermo Fisher, AM9765)) followed by the addition of the gene library mix for the hybridization step (48 h, 37 °C). Samples were then washed twice with Formamide Wash Buffer (2x, 30 min, 47 °C), and then embedded in a gel embedding solution (0.5% of 10% w/v ammonium persulfate, 0.05% TEMED, 4% 19:1 acrylamide/bis-acrylamide solution, 0.3 M NaCl, 0.06 M Tris PH8), followed by overnight incubation with tissue clearing solution (2X SSC, 2% SDS, 0.5% v/v Triton X-100, and proteinase K 1:100) at 37 °C. Finally, samples are washed, incubated with DAPI and polyT solution (15 min RT), and washed with formamide wash buffer (10 min RT).

The MERSCOPE 500 gene imaging kit was activated by adding 250 µL of Imaging Buffer Activator (Vizgen, #203000015) and 100 µL of RNAse Inhibitor (New England BioLabs, M0314L). 15 ml of mineral oil was overlaid on top of the imaging buffer through the activation port. After instrument priming and chamber assembly as per MERSCOPE user guide, a 10x low resolution mosaic was acquired for imaging area selection. Raw data was decoded using Vizgen's analyzing pipeline incorporated in the MERSCOPE. Vizgen's postprocessing tool (Vizgen, Cambridge, MA) was then applied to obtain the cell segmentation based on the DAPI staining by using the CellPose algorithm. Segmentation was performed on the middle Z plane (3rd out of 7) and cell borders were propagated to z-planes above and below. MERFISH processed data was analyzed in RStudio using Seurat 4.1.3, R 4.2.2 and custom-made scripts. Cell filtering was applied to the dataset to remove cells < 50 μm^3 and < 10 unique transcripts and < 10 transcript counts. Cell gene expression per cell was then normalized to each cell's volume and the mean RNA per sample. To perform cell clustering we followed a modified Seurat pipeline. We performed principal component analysis (PCA) with 400 genes as the variable features followed by dimensionality analysis with a resolution of 1.45 and 20 dimensions. Dimensionality reduction was performed with Uniform Manifold Approximation and Projection (UMAP). Cell clusters were manually annotated according to the expression of widely used cell-type specific gene markers as well as spatial distribution.

For quality control, there were 62 "blank" barcodes or negative control probes, which are probes that do not correspond to any specific RNA in our library. Out of the 62 blank barcodes, 95.15% were not differentially expressed between the old and young samples. Out of the three blank barcodes that are differentially expressed between old and young conditions, two are upregulated and one downregulated, further supporting that there is not an increase of probe identification in either condition and that there was not a random increase in gene detection in one condition vs the other. For housekeeping genes, when we compared the cells within the lesion and non-lesion areas in the old and young conditions, we observed that *Tmem119, Aldhl1l, Plp1, Cspg4, Pdgfra, Pecam1* and *Cldn5*, all cell type markers used to identify the observed populations, are not differentially expressed when young and old conditions are compared, further supporting that the observed differences are biologically meaningful.

Re-analysis of Human MS snRNA-sequencing data

The published single nucleus dataset of the human MS brain (PRJNA544731) was used to validate the expression of the *p16/Cdkn2a* gene. The ambient RNA, a pervasive artifact in single nucleus datasets, was removed from the raw data using CellBender (v0.3.0, https://github.com/broadinstitute/CellBender)[84], specifically the cellbender-remove background function including 50,000 droplets (total-droplets-included 50,000). The subsequent quality control, dimensionality reduction and clustering were performed using Seurat (v5.0, https://github.com/satijalab/seurat)[85], in the R statistical environment

(v4.1.2). The filtered CellBender output was read into Seurat using the Read10X_h5() function and a SeuratObject was created using the CreateSeuratObject() function, retaining only the cells expressing at least 200 genes and genes expressed in at least 3 cells. The remaining 26,201 genes and 49,995 cells were further filtered to exclude doublets/multiplets by removing cells with high gene counts (>7500) and dead cells by removing cells with a high proportion of mitochondrial genes (>10%). The dataset was normalized using the SCTransform() function according to the binomial regression model[86] (Highly variable features = 3000, regressed nCount and mitochondrial genes). The dimensionality reduction was performed using RunPCA(), FindNeighbors() (Dimensions = 20) and FindClusters() functions. Twenty-five PCs were used for downstream analyses as determined by the PCA elbow plot (min.dist = 0.3). The optimal clustering resolution was determined to be 0.5 using the Clustree package (v0.5.1, https://github.com/lazappi/clustree)[87]. The FindClusters() function was used to cluster the dataset at 11 resolutions ranging from 0 to 1, separated by 0.1 All resolutions were plotted on a tree generated through by clustree() function and 0.5 was identified as the most stable clustering level. The microglia ($n = 1815$) were subsetted using the subset() function based on *TMEM119*/*P2RY12* expression and clustered again as described above. The differential gene expression was determined using the FindMarkers() function. The SeuratObject was converted to an h5ad object using SeuratDisk by converting the RDS object to an h5Seurat object using the Saveh5Seurat() function and converting the h5Seurat object to an h5ad object using the convert() function (Destination = h5ad). The h5ad file was read into a Jupyter notebook (v6.0.3) running a python environment (Python 3.8.3) using Scanpy (v1.6.0, https://github.com/scverse/scanpy)[88]. The final clustering was projected onto a UMAP using the pl.umap() function and the genes were plotted using the pl.violin() function. The senescence score was calculated by aggregate sum expression of CDKN2A, CDKN1A, CDKN2D, CASP8, IL1B, GLB1, SERPINE1, AXL, BCL2A1A, CCL3, CCL4, CCL5, CENPB, CSF1, ITGAX, SPP1, TGFB1, TMEM173, VIM, BCL2, TNFRSF1A. The kernel density was plotted using the plot_density function of the Nebulosa package (v1.4.0)[89].

Re-analysis of mouse lesion snRNA-sequencing data

The recently generated single-nucleus RNA-sequencing single nucleus dataset of mouse LPC-lesioned tissue undergoing remyelination[31] was used to validate senescence expression and myelin gene expression over time, as well as D/Q target genes. Briefly, processed data (GSE278643) were directly downloaded, and all quality control, dimensionality reduction, and clustering were performed using Seurat (v5.1.0) in R (v4.4.1) following the same standards as the original publication. These included filtering using *ddqc*[90] such that on a cluster-by-cluster basis nuclei with nUMI>500 and 300<nGene<3-MADs were retained. Further filtration utilized universal standards of mitochondrial gene counts < 1% and ribosomal gene counts <5%. Filtration resulted in a total of 48,255 nuclei merged across all samples (naïve spinal cord tissue ($n = 2$), lesioned spinal cord tissue at 5dpl ($n = 3$), 10dpl ($n = 2$), and 20dpl ($n = 3$)), which were utilized in downstream analyses in this study. To cluster the data, we utilized the SCTransform() function[86]. The dataset count matrix was also log normalized using the NormalizeData() function to identify cluster gene markers. All cell populations were annotated based off of well-known and calculated marker genes through the FindAllMarkers() function. Oligodendrocyte lineage cells (*Pdgfra*, *Bcas1*, *Mobp*, *Plp1*) and myeloid cells (*Cx3cr1*, *P2ry12*, *Ptprc*) were subset based off respective marker genes. Subset datasets were reclustered and filtered following the original publication, and count matrices were renormalized using the NormalizeData() function. SenMayo scores are based off the SenMayo senescence geneset[32]. Scores were calculated by the aggregate normalized sum expression of the SenMayo genes found in the overall dataset per nuclei barcode (113 genes, Supplementary data 1), and were plotted using scCustomize (v2.1.2, DOI: 10.5281/zenodo.5706430). For violin plots of geneset scores, single nuclei were randomly downsampled as detailed in individual figure legends. For statistical comparisons, the number of nuclei/timepoint were used. *P*-values in violin plots were calculated using compare_means() from the ggpubr package (v0.6.0), using the Wilcoxon non-parametric test followed by Bonferroni correction for multiple comparisons. *P*-values were then plotted using stat_pvalue_manual() from the ggpubr package (v0.6.0). Line graphs were made using ggplot2 (v3.5.1) in R (4.4.1). Mean gene expression was calculated for all selected genes and then normalized by subtracting the mean gene expression of each respective gene from either the naïve condition or 5dpl condition, as detailed in individual plot figure legends. Confidence intervals (95%) were calculated and were plotted in the line graphs using the geom_ribbon() function.

Primary rat oligodendrocyte culture, CCL11 treatment, and staining

Oligodendrocyte precursor cells (OPCs) were purified from Sprague-Dawley rat pups (P6–P8) (Charles River) of both genders by immunopanning as previously described in ref. 91. Briefly, cortical tissue was dissociated by papain digestion then filtered through a 40 μm cell strainer to obtain a single-cell suspension. This suspension was incubated in two negative-selection plates, one coated with anti-Ran-2 antibody and the other coated anti-GC (glucocerebrosidase) antibody, then in a positive-selection plate coated with anti-O4 antibody. Adherent cells were trypsinized and plated on 12 mm glass coverslips sonicated for 1 h in ethanol and coated with poly-D-lysine (PDL) hydrobromide at a density of 10,000–20,000 cells per coverslip. Cells were cultured at 37 °C in rat OPC differentiation media containing T3. At DIV 2 and 4, cells were treated with either vehicle (PBS containing 0.1% BSA) or recombinant mCCL11 (100 ng/μL[54,59], R&D Systems #420-ME-020/CF), then fixed on DIV5 with 4% paraformaldehyde for 10 min, permeabilized with 0.1% Triton X-100 in PBS for 3 min, then blocked with 5% donkey serum with 1% BSA in PBS for 30 min. Primary antibody incubation was performed at 4 °C overnight using the following antibodies and dilutions: MBP (Abcam ab7349, 1:100), O4 (R&D Systems MAB1326, 1:250), α/β-tubulin (Cytoskeleton, Inc ATN-02, 1:200). Secondary antibody incubation was performed at room temperature for 1 h. Samples were imaged on a spinning disk confocal (Nikon Eclipse-T2 inverted microscope with Yokogawa X1 spinning disk) with a sCMOS camera (Hamamatsu Orca-FusionBT).

Oligodendrocyte culture quantification and statistical analysis

MBP expression analysis was performed manually, with sample conditions blinded. Cells with relatively little or no MBP signal were marked as "low" MBP expressors. GraphPad Prism 10 was used for statistical analysis. First, tests of parametricity were used (D'Agostino & Pearson; Anderson-Darling; Shapiro-Wilk; Kolmogorov-Smirnov), then analyzed by t-test (Kolmogorov-Smirnov test). All data and error bars are presented as SEM (standard error of the mean).

Human Samples

Recruitment was done at Rocky Mountain Multiple Sclerosis Center Biorepository at University of Colorado Anschutz Medical Campus, upon Institutional Review Board approval (COMIRB 12-0968) and after written informed consent. Blood was collected as part of standard of care procedures in two 15 mL glass vacutainers containing 1.5 mL 3.8% Sodium Citrate solution. Both vacutainers were then pooled together in a 50 mL Leucosep tube (Greiner Bio-One) filled with 15 mL Lymphoprep (Stemcell). The Leucosep tube was then centrifuged at 1800 x g for 15 min at half brake. After centrifugation, plasma was then removed from above the mononuclear cell layer and transferred into a 15 mL conical. Plasma was then centrifuged at 500 x g for 10 min at full brake. Plasma was then aliquoted and transferred to −80 °C for storage.

ELISAs
CCL11 was measured in blood plasma from healthy controls and MS patients according to the manufacturer's protocol (R&D Systems, #DTX00). The study involved both females and males with a female:male ratio of 3:1, due to the disease being more prevalent in women. Participants self-reported their sex and gender identity. Sex was not included in the analyses as a covariate to adjust for any effects it may have. The results may apply to both females and males.

Data analyses
All statistics were performed in GraphPad Prism 10. Data is presented as mean ± SEM. Each value represents an individual biological sample, where technical replicates have been averaged. Statistical significance is reported as: ns ($p > 0.05$), * ($p < 0.05$), ** ($p < 0.01$), *** ($p < 0.001$), **** ($p < 0.0001$).

Reporting summary
Further information on research design is available in the Nature Portfolio Reporting Summary linked to this article.

Data availability
The data generated in this study are provided in the Source Data file. The RNA sequencing, MERFISH, and Melchor et al. [31] raw data used in this study are available in the Gene Expression Omnibus (GEO) database under accession code GSE268386, GSE268492, and GSE278643. Source data are provided with this paper.

Code availability
Analysis code for MERFISH was deposited at: https://github.com/SchaferLabUMassChan/Gross_2024.

References

1. Reich, D. S., Lucchinetti, C. F. & Calabresi, P. A. Multiple Sclerosis. *N. Engl. J. Med.* **378**, 169–180 (2018).
2. Franklin, R. J. M. & Ffrench-Constant, C. Remyelination in the CNS: From biology to therapy. *Nat. Rev. Neurosci.* **9**, 839–855 (2008).
3. Franklin, R. J. M., Zhao, C. & Sim, F. J. Ageing and CNS remyelination. *Neuro. Rep.* **13**, 923–928 (2002).
4. Neumann, B., Segel, M., Chalut, K. J. & Franklin, R. J. Remyelination and ageing: Reversing the ravages of time. *Mult. Scler. J.* **25**, 1835–1841 (2019).
5. Graves, J. S., et al. Ageing and multiple sclerosis. *Lancet Neurol.* S1474442222001843 https://doi.org/10.1016/S1474-4422(22)00184-3 (2022).
6. Scalfari, A., Neuhaus, A., Daumer, M., Ebers, G. C. & Muraro, P. A. Age and disability accumulation in multiple sclerosis. *Neurology* **77**, 1246–1252 (2011).
7. Goldschmidt, T., Antel, Konig, Bruck & Kuhlmann, T. Remyelination capacity of the MS brain decreases with disease chronicity. *Neurology* **72**, 1914–1921 (2009).
8. Tutuncu, M. et al. Onset of progressive phase is an age-dependent clinical milestone in multiple sclerosis. *Mult. Scler. J.* **19**, 188–198 (2013).
9. Zeydan, B. & Kantarci, O. H. Impact of Age on Multiple Sclerosis Disease Activity and Progression. *Curr. Neurol. Neurosci. Rep.* **20**, 1–7 (2020).
10. Conway, B. L. et al. Age is a critical determinant in recovery from multiple sclerosis relapses. *Mult. Scler. J.* **25**, 1754–1763 (2019).
11. Weideman, A. M., Tapia-Maltos, M. A., Johnson, K., Greenwood, M. & Bielekova, B. Meta-analysis of the age-dependent efficacy of multiple sclerosis treatments. *Front. Neurol.* **8**, 1–12 (2017).
12. Hayflick, L. The limited in vitro lifetime of human diploid cell strains. *Exp. Cell Res.* **37**, 614–636 (1965).
13. Coppé, J.-P., Desprez, P.-Y., Krtolica, A. & Campisi, J. The Senescence-Associated Secretory Phenotype: The Dark Side of Tumor Suppression. https://doi.org/10.1146/annurev-pathol-121808-102144 (2010).
14. Campisi, J. et al. From discoveries in ageing research to therapeutics for healthy ageing. *Nature* **571**, 183–192 (2019).
15. Baker, D. J. & Petersen, R. C. Cellular senescence in brain aging and neurodegenerative diseases: evidence and perspectives. *J. Clin. Invest.* **128**, 1208–1216 (2018).
16. Bussian, T. J. et al. Clearance of senescent glial cells prevents tau-dependent pathology and cognitive decline. *Nature* **562**, 578–582 (2018).
17. Zhang, P. et al. Senolytic therapy alleviates Aβ-associated oligodendrocyte progenitor cell senescence and cognitive deficits in an Alzheimer's disease model. *Nat. Neurosci.* **22**, 1 (2019).
18. Aguado, J. et al. Senolytic therapy alleviates physiological human brain aging and COVID-19 neuropathology. *Nat. Aging* **3**, 1561–1575 (2023).
19. Baker, D. J. et al. Clearance of p16 Ink4a-positive senescent cells delays ageing-associated disorders. https://doi.org/10.1038/nature10600 (2012).
20. Suda, M. et al. Senolytic vaccination improves normal and pathological age-related phenotypes and increases lifespan in progeroid mice. *Nat. Aging* **1**, 1117–1126 (2021).
21. Xu, M. et al. Senolytics improve physical function and increase lifespan in old age. *Nat. Med.* **24**, 1246–1256 (2018).
22. Baker, D. J. et al. Naturally occurring p16Ink4a-positive cells shorten healthy lifespan. *Nature* **530**, 184–189 (2016).
23. Høgestøl, E. A. et al. Cross-Sectional and Longitudinal MRI Brain Scans Reveal Accelerated Brain Aging in Multiple Sclerosis. *Front. Neurol.* **10**, 450 (2019).
24. Nicaise, A. M. et al. Cellular senescence in progenitor cells contributes to diminished remyelination potential in progressive multiple sclerosis. *Proc. Natl. Acad. Sci. USA.* **116**, 201818348 (2019).
25. Absinta, M. et al. A lymphocyte–microglia–astrocyte axis in chronic active multiple sclerosis. *Nature* **597**, 709–714 (2021).
26. Ionescu, R.-B. et al. Increased cholesterol synthesis drives neurotoxicity in patient stem cell-derived model of multiple sclerosis. *Cell Stem Cell* **31**, 1574–1590.e11 (2024).
27. Drake, S. S. et al. Senolytic treatment diminishes microglia and decreases severity of experimental autoimmune encephalomyelitis. *J. Neuroinflamm.* **21**, 283 (2024).
28. Baydyuk, M. et al. Tracking the evolution of CNS remyelinating lesion in mice with neutral red dye. *Proc. Natl. Acad. Sci. USA.* **116**, 14290–14299 (2019).
29. Keough, M. B., Jensen, S. K. & Yong, V. W. Experimental Demyelination and Remyelination of Murine Spinal Cord by Focal Injection of Lysolecithin. *J. Vis. Exp.* 52679. https://doi.org/10.3791/52679 (2015).
30. Liu, J. Y. et al. Cells exhibiting strong p16 INK4a promoter activation in vivo display features of senescence. *Proc. Natl. Acad. Sci. Usa.* **116**, 2603–2611 (2019).
31. Melchor, G. S., Baydyuk, M., Manavi, Z., Hu, J. & Huang, J. K. Dissecting the evolving cellular landscape of a remyelinating microenvironment. *BioRxiv.* https://doi.org/10.1101/2024.12.25.630253 (2024).
32. Saul, D. et al. A new gene set identifies senescent cells and predicts senescence-associated pathways across tissues. *Nat. Commun.* **13**, 4827 (2022).
33. Baaklini, C. S. et al. Microglia promote remyelination independent of their role in clearing myelin debris. *Cell Rep.* **42**, 113574 (2023).
34. Plemel, J. R. et al. Microglia response following acute demyelination is heterogeneous and limits infiltrating macrophage dispersion. *Sci. Adv.* **6**, 1–16 (2020).
35. Buttgereit, A. et al. Sall1 is a transcriptional regulator defining microglia identity and function. *Nat. Immunol.* **17**, 1397–1406 (2016).

36. Schirmer, L. et al. Neuronal vulnerability and multilineage diversity in multiple sclerosis. *Nature* **573**, 75–82 (2019).
37. Hu, Y. et al. Replicative senescence dictates the emergence of disease-associated microglia and contributes to Aβ pathology. *Cell Rep* **35**, 109228 (2021).
38. Casella, G. et al. Transcriptome signature of cellular senescence. *Nucleic Acids Res.* **47**, 7294–7305 (2019).
39. Hernandez-Segura, A. et al. Unmasking Transcriptional Heterogeneity in Senescent Cells. *Curr. Biol.* **27**, 2652–2660.e4 (2017).
40. Keren-Shaul, H. et al. A Unique Microglia Type Associated with Restricting Development of Alzheimer's Disease. *Cell* **169**, 1276–1290.e17 (2017).
41. Krasemann, S. et al. The TREM2-APOE Pathway Drives the Transcriptional Phenotype of Dysfunctional Microglia in Neurodegenerative Diseases. *Immunity* **47**, 566–581.e9 (2017).
42. Zhang, X. et al. Rejuvenation of the aged brain immune cell landscape in mice through p16-positive senescent cell clearance. *Nat. Commun.* **13**, 5671 (2022).
43. Carver, C. et al. *Senescent and Disease-Associated Microglia Are Modifiable Features of Aged Brain White Matter*. https://doi.org/10.21203/rs.3.rs-3467812/v1 (2023).
44. Li, Q. et al. Interferon Regulatory Factors IRF5 and IRF7 Inhibit Growth and Induce Senescence in Immortal Li-Fraumeni Fibroblasts. *Mol. Cancer Res.* **6**, 770–784 (2008).
45. Burton, D. G. A. et al. Cyclin D1 Overexpression Permits the Reproducible Detection of Senescent Human Vascular Smooth Muscle Cells. *Ann. N.Y. Acad. Sci.* **1119**, 20–31 (2007).
46. Zhu, Y. et al. The Achilles' heel of senescent cells: from transcriptome to senolytic drugs. *Aging Cell* **14**, 644–658 (2015).
47. Sim, F. J., Zhao, C., Penderis, J. & Franklin, R. J. M. The Age-Related Decrease in CNS Remyelination Efficiency Is Attributable to an Impairment of Both Oligodendrocyte Progenitor Recruitment and Differentiation. *J. Neurosci.* **22**, 2451–2459 (2002).
48. Sim, F. J., Hinks, G. L. & Franklin, R. J. M. The re-expression of the homeodomain transcription factor Gtx during remyelination of experimentally induced demyelinating lesions in young and old rat brain. *Neuroscience* **100**, 131–139 (2000).
49. Woodruff, R. H. & Franklin, R. J. M. Demyelination and remyelination of the caudal cerebellar peduncle of adult rats following stereotaxic injections of lysolecithin, ethidium bromide, and complement/anti-galactocerebroside: A comparative study. *Glia* **25**, 216–228 (1999).
50. Gonzales, M. M. et al. Senolytic therapy in mild Alzheimer's disease: a phase 1 feasibility trial. *Nat. Med.* **29**, 2481–2488 (2023).
51. Psenicka, M. W., Smith, B. C., Tinkey, R. A. & Williams, J. L. Connecting Neuroinflammation and Neurodegeneration in Multiple Sclerosis: Are Oligodendrocyte Precursor Cells a Nexus of Disease? *Front. Cell. Neurosci.* **15**, 654284 (2021).
52. Hoefer, J. et al. The "Aging Factor" Eotaxin-1 (CCL11) Is Detectable in Transfusion Blood Products and Increases with the Donor's Age. *Front. Aging Neurosci.* **9**, 402 (2017).
53. Tashiro, R. et al. Young Astrocytic Mitochondria Attenuate the Elevated Level of CCL11 in the Aged Mice, Contributing to Cognitive Function Improvement. *Int. J. Mol. Sci.* **24**, 5187 (2023).
54. Villeda, S. A. et al. The ageing systemic milieu negatively regulates neurogenesis and cognitive function. *Nature* **477**, 90–94 (2011).
55. Lavandoski, P. et al. Eotaxin-1/CCL11 promotes cellular senescence in human-derived fibroblasts through pro-oxidant and pro-inflammatory pathways. *Front. Immunol.* **14**, 1243537 (2023).
56. Erickson, M. A., Morofuji, Y., Owen, J. B. & Banks, W. A. Rapid Transport of CCL11 across the Blood-Brain Barrier: Regional Variation and Importance of Blood Cells. *J. Pharmacol. Exp. Ther.* **349**, 497–507 (2014).
57. Huber, A. K., Giles, D. A., Segal, B. M. & Irani, D. N. An emerging role for eotaxins in neurodegenerative disease. *Clin. Immunol.* **189**, 29–33 (2018).
58. Fernández-Castañeda, A. et al. Mild respiratory COVID can cause multi-lineage neural cell and myelin dysregulation. *Cell* **185**, 2452–2468.e16 (2022).
59. Büttner, R. et al. Inflammaging impairs peripheral nerve maintenance and regeneration. *Aging Cell* **17**, e12833 (2018).
60. Maysami, S. et al. Oligodendrocyte precursor cells express a functional chemokine receptor CCR3: Implications for myelination. *J. Neuroimmunol.* **178**, 17–23 (2006).
61. Tejera-Alhambra, M. et al. Plasma Biomarkers Discriminate Clinical Forms of Multiple Sclerosis. *PLOS ONE* **10**, e0128952 (2015).
62. Huang, J. et al. Inflammation-related plasma and CSF biomarkers for multiple sclerosis. *Proc. Natl. Acad. Sci.* **117**, 12952–129960 (2020).
63. Demaria, M. et al. An essential role for senescent cells in optimal wound healing through secretion of PDGF-AA. *Dev. Cell* **31**, 722–733 (2014).
64. Chiche, A. et al. Injury-Induced Senescence Enables In Vivo Reprogramming in Skeletal Muscle. *Cell Stem Cell* **20**, 407–414.e4 (2017).
65. Yao, H. et al. Timing and cell specificity of senescence drives postnatal lung development and injury. *Nat. Commun.* **14**, 273 (2023).
66. Paramos-de-Carvalho, D. et al. Targeting senescent cells improves functional recovery after spinal cord injury. *Cell Rep* **36**, 109334 (2021).
67. Moiseeva, V. et al. Senescence atlas reveals an aged-like inflamed niche that blunts muscle regeneration. *Nature* **613**, 169–178 (2022).
68. Van Deursen, J. M. The role of senescent cells in ageing. *Nature* **509**, 439–446 (2014).
69. Furman, D. et al. Chronic inflammation in the etiology of disease across the life span. *Nat. Med.* **25**, 1822–1832 (2019).
70. Segel, M. et al. Niche stiffness underlies the ageing of central nervous system progenitor cells. *Nature* **573**, 130–134 (2019).
71. Rawji, K. S., Neumann, B. & Franklin, R. J. M. Glial aging and its impact on central nervous system myelin regeneration. *Ann. N.Y. Acad. Sci.* nyas.14933. https://doi.org/10.1111/nyas.14933 (2022).
72. Chari, D. M., Crang, A. J. & Blakemore, W. F. Decline in Rate of Colonization of Oligodendrocyte Progenitor Cell (OPC)-Depleted Tissue by Adult OPCs with Age. *J. Neuropathol. Exp. Neurol.* **62**, 908–916 (2003).
73. Neumann, B. et al. Metformin Restores CNS Remyelination Capacity by Rejuvenating Aged Stem Cells. *Cell Stem Cell* **25**, 473–485.e8 (2019).
74. Behmoaras, J. & Gil, J. Similarities and interplay between senescent cells and macrophages. *J. Cell Biol.* **220**, e202010162 (2021).
75. Talma, N., Gerrits, E., Wang, B., Eggen, B. J. L. & Demaria, M. Identification of distinct and age-dependent p16 High microglia subtypes. *Aging Cell* **20**, e13450 (2021).
76. Ogrodnik, M. et al. Guidelines for minimal information on cellular senescence experimentation in vivo. *Cell* **187**, 4150–4175 (2024).
77. Ng, P. Y., Zhang, C., Li, H. & Baker, D. J. Senescent Microglia Represent a Subset of Disease-Associated Microglia in P301S Mice. *J. Alzheimers Dis.* **95**, 493–507 (2023).
78. Rachmian, N. et al. Identification of senescent, TREM2-expressing microglia in aging and Alzheimer's disease model mouse brain. *Nat. Neurosci.* **27**, 1116–1124 (2024).
79. Matsudaira, T. et al. Cellular senescence in white matter microglia is induced during ageing in mice and exacerbates the neuroinflammatory phenotype. *Commun. Biol.* **6**, 665 (2023).
80. Zia, S. et al. Single-cell microglial transcriptomics during demyelination defines a microglial state required for lytic carcass clearance. *Mol. Neurodegener.* **17**, 82 (2022).
81. Nugent, A. A. et al. TREM2 Regulates Microglial Cholesterol Metabolism upon Chronic Phagocytic Challenge. *Neuron* **105**, 837–854.e9 (2020).

82. Herr, L. M., Schaffer, E. D., Fuchs, K. F., Datta, A. & Brosh, R. M. Replication stress as a driver of cellular senescence and aging. *Commun. Biol.* **7**, 616 (2024).
83. Kaiser, T. et al. MyelTracer: A Semi-Automated Software for Myelin *g* -Ratio Quantification. *eneuro* **8**, ENEURO.0558-20.2021 (2021).
84. Fleming, S. J. et al. Unsupervised removal of systematic background noise from droplet-based single-cell experiments using CellBender. *Nat. Methods* **20**, 1323–1335 (2023).
85. Hao, Y. et al. Integrated analysis of multimodal single-cell data. *Cell* **184**, 3573–3587.e29 (2021).
86. Hafemeister, C. & Satija, R. Normalization and variance stabilization of single-cell RNA-seq data using regularized negative binomial regression. *Genome Biol* **20**, 296 (2019).
87. Zappia, L., Phipson, B. & Oshlack, A. Exploring the single-cell RNA-seq analysis landscape with the scRNA-tools database. *PLOS Comput. Biol.* **14**, e1006245 (2018).
88. Wolf, F. A., Angerer, P. & Theis, F. J. SCANPY: large-scale single-cell gene expression data analysis. *Genome Biol* **19**, 15 (2018).
89. Alquicira-Hernandez, J. & Powell, J. E. Nebulosa recovers single-cell gene expression signals by kernel density estimation. *Bioinformatics* **37**, 2485–2487 (2021).
90. Subramanian, A., Alperovich, M., Yang, Y. & Li, B. Biology-inspired data-driven quality control for scientific discovery in single-cell transcriptomics. *Genome Biol* **23**, 267 (2022).
91. Dugas, J. C. & Emery, B. Purification of Oligodendrocyte Precursor Cells from Rat Cortices by Immunopanning. *Cold Spring Harb. Protoc.* **2013**, 745–758 (2013).

Acknowledgements

P.S.G. was supported by the Center for Neural Injury and Recovery (CNIR) program (NINDS/NIH T32NS041218). J.K.H. was supported by NIA/NIH (R21AG072327), NINDS/NIH (R01NS107523), and NMSS Harry Weaver Neuroscience Scholar Award (JF-1806-31381). D.P.S was supported by NIMH/NIH (R01MH113743), NINDS/NIH (R01NS117533), NIA/NIH (RF1AG068281), NIH (R24OD036199), and the Miriam and Sheldon G. Adelson Medical Research Foundation (DPS). V.D.L was supported by BrightFocus Foundation (A2022006F) and Alzheimer's Association AARF-22-923219. S.S. was supported by the Rocky Mountain Multiple Sclerosis Center. We would like to thank Olga Rodriguez, MD, PhD from the Preclinical Imaging Research Laboratory (PIRL) at Georgetown University Medical Center for training on the In Vivo Imaging System (IVIS) imager. We would also like to acknowledge Eve Technologies and Azenta Life Sciences for their services.

Author contributions

P.S.G. and J.K.H. designed the study. P.S.G. performed all animal and human sample experiments and interpreted the data. Z.M. and S.H.L. contributed intellectually and assisted in animal experiments. V.D.L. processed the MERFISH data and developed the computational framework and performed associated analyses. P.S.G. and V.D.L. interpreted the MERFISH data. D.P.S. oversaw the MERFISH experiments. N.S. performed SEM imaging. L.T.H. and W.E.B. performed the in vitro oligodendrocyte experiments and M.M.F. oversaw the in vitro experiments. S.Z. performed re-analysis of MS snRNAseq data and J.R.P. oversaw the snRNAseq re-analysis. G.S.M. performed re-analysis of mouse snRNAseq lesion data. S.S. and E.A. isolated and provided human blood plasma samples. P.S.G. wrote the original draft of the manuscript. J.K.H. contributed to data interpretation, edited the manuscript, and oversaw the study. All authors discussed the results and reviewed the manuscript.

Competing interests

The authors declare no competing interests.

Additional information

Supplementary information The online version contains supplementary material available at https://doi.org/10.1038/s41467-025-57632-w.

Correspondence and requests for materials should be addressed to Jeffrey K. Huang.

Peer review information *Nature Communications* thanks the anonymous reviewer(s) for their contribution to the peer review of this work. A peer review file is available.

Reprints and permissions information is available at http://www.nature.com/reprints

Publisher's note Springer Nature remains neutral with regard to jurisdictional claims in published maps and institutional affiliations.

Open Access This article is licensed under a Creative Commons Attribution-NonCommercial-NoDerivatives 4.0 International License, which permits any non-commercial use, sharing, distribution and reproduction in any medium or format, as long as you give appropriate credit to the original author(s) and the source, provide a link to the Creative Commons licence, and indicate if you modified the licensed material. You do not have permission under this licence to share adapted material derived from this article or parts of it. The images or other third party material in this article are included in the article's Creative Commons licence, unless indicated otherwise in a credit line to the material. If material is not included in the article's Creative Commons licence and your intended use is not permitted by statutory regulation or exceeds the permitted use, you will need to obtain permission directly from the copyright holder. To view a copy of this licence, visit http://creativecommons.org/licenses/by-nc-nd/4.0/.

© The Author(s) 2025